
DIFFUSION MODELS FOR MULTIVARIATE SUBSURFACE GENERATION AND EFFICIENT PROBABILISTIC INVERSION

Roberto Miele
 Institute of Earth Sciences
 University of Lausanne
 Lausanne, Switzerland
 roberto.miele@unil.ch

Niklas Linde
 Institute of Earth Sciences
 University of Lausanne
 Lausanne, Switzerland
 niklas.linde@unil.ch

September 24, 2025

ABSTRACT

Diffusion models offer stable training and state-of-the-art performance for deep generative modeling tasks. Here, we consider their use in the context of multivariate subsurface modeling and probabilistic inversion. We first demonstrate that diffusion models enhance multivariate modeling capabilities compared to variational autoencoders and generative adversarial networks. In diffusion modeling, the generative process involves a comparatively large number of generative steps with update rules that can be modified to account for conditioning data. We propose different corrections to the popular Diffusion Posterior Sampling approach by Chung et al. (2023). In particular, we introduce a likelihood approximation accounting for the noise-contamination that is inherent in diffusion modeling. We assess performance in a multivariate geological scenario involving facies and correlated acoustic impedances. Conditional modeling is demonstrated using both local hard data (well logs) and nonlinear geophysics (fullstack seismic data). Our tests show significantly improved statistical robustness, enhanced sampling of the posterior probability density function and reduced computational costs, compared to the original approach. The method can be used with both hard and indirect conditioning data, individually or simultaneously. As the inversion is included within the diffusion process, it is faster than other methods requiring an outer-loop around the generative model, such as Markov chain Monte Carlo.

Keywords Diffusion models · Diffusion Posterior Sampling · Bayesian inversion · Geophysics · Multivariate modeling · Subsurface characterization

1 Introduction

Predicting the spatial distribution of subsurface properties is a key challenge in the Earth and environmental sciences. Probabilistic inverse modeling [Grana et al., 2021, Rubin and Hubbard, 2005] aims to approximate the posterior probability density function (pdf) by integrating prior pdfs with observed data in the form of a likelihood function [Tarantola, 2005]. Conditioning data may consist of local measurements (e.g., well logs) or indirect geophysical data describing averaged subsurface properties through linear or nonlinear physical forward operators. Prior pdfs expressed as explicit statistical models (e.g., two-point geostatistical models) are computationally convenient, yet are often gross simplifications of geological heterogeneity, leading to biased predictions and incomplete uncertainty quantification [e.g., Linde et al., 2017, Gómez-Hernández and Wen, 1998, Neuweiler et al., 2011, Journel and Deutsch, 1993, Zhou et al., 2018]. Alternatively, prior geological knowledge can be represented using 2D or 3D gridded data, defined as training images (TI) that implicitly describe lower- and higher-order spatial relationships. Multiple-Point Statistics (MPS) simulation methods [Guardiano and Srivastava, 1993, Strebelle, 2002, Mariethoz et al., 2010a, Mariethoz and Caers, 2014] rely on TIs to draw geologically-realistic model realizations and have found wide applicability in both hydro-geology [e.g., Høyer et al., 2017, Le Coz et al., 2017, Straubhaar et al., 2020] and reservoir characterization [e.g., Melnikova et al., 2015, Caers and Zhang, 2004, & references therein]. These realizations can easily be made to

honor local observations [Straubhaar et al., 2016, Hansen et al., 2018, Straubhaar and Renard, 2021], but struggle with high computational costs and poor posterior exploration when used in the context of nonlinear inversion [e.g., Zahner et al., 2016, Levy et al., 2024, Laloy et al., 2016, Hansen et al., 2012, Mariethoz et al., 2010b].

The substantial progress of deep generative models over the past decade [Goodfellow et al., 2016] have created a strong interest in leveraging such techniques in the geosciences. Initial work considered convolution-based deep neural networks, such as variational autoencoders [VAE; Kingma and Welling, 2013] and generative adversarial networks [GAN; Goodfellow et al., 2014]. These methods can encode complex geological patterns of a TI within a low-dimensional manifold, defining prior pdfs [Laloy et al., 2017, 2018]. Inversion can then be performed within the latent space of the pre-trained networks [Laloy et al., 2017, 2018, Oliviero-Durmus et al., 2025] using sampling methods, such as Markov chain Monte Carlo [MCMC; Laloy et al., 2017, 2018, Levy et al., 2021, Mosser et al., 2020, Liu et al., 2022] and Sequential Monte Carlo [SMC; Doucet et al., 2001, Amaya et al., 2021], ensemble-based approaches [Canchumuni et al., 2019, Liu and Grana, 2020, Mo et al., 2020], deterministic optimization [Laloy et al., 2019, Dupont et al., 2018], or variational inference [Chan and Elsheikh, 2019, Levy et al., 2023, Miele et al., 2024]. Contrarily to MPS algorithms, conditioning to local data remains cumbersome. One can train the generative models as inference methods on specific conditional data, but this necessitates retraining for each application task [e.g. Mosser et al., 2018, Zhang et al., 2021, Laloy et al., 2020, Feng et al., 2024, Miele and Azevedo, 2024]. Moreover, GANs are prone to unstable training and mode collapse [e.g., Lucic et al., 2018], and the non-linearity of the generative process often adversely affects the inversion results [Laloy et al., 2019, Lopez-Alvis et al., 2021]. Formulations based on VAEs are more stable, but offer rather lossy representations [e.g., Levy et al., 2023, Miele et al., 2024].

Diffusion models [DM; Ho et al., 2020, Sohl-Dickstein et al., 2015] represent the current state-of-the-art in deep generative modeling, outperforming GANs in terms of accuracy without being affected by mode collapse or unstable training [e.g., Dhariwal and Nichol, 2021]. These methods are based on reversing a *data corruption* process transforming samples of a target distribution (the TI) into those of a known distribution (typically Gaussian). The generative process involves iteratively denoising samples originating from the latter, with the denoising trajectory being learned by a deep neural network [e.g., Ho et al., 2020, Song et al., 2021a,b, Karras et al., 2022].

In geological subsurface modeling, diffusion models (DMs) have been explored in different contexts. Mosser [2023] showed that autoregressive DMs [Hoogeboom et al., 2022] share structural similarities with sequential geostatistical modeling and demonstrated their potential for simulating multi-scale 2D synthetic channel patterns. Xu et al. [2024] found high modeling accuracy of DMs in analogous geological scenarios and proposed a conditional generative approach, where sparse point observations were incorporated as input channels during training. Aouf et al. [2025] demonstrated that DMs can be used for 2D and 3D modeling of complex porous geological media, further performing conditional modeling on total porosity values, by training the DM to embed such conditioning parameter and associate it to the desired output. Conditioning on embedded well-log data was further investigated by Lee et al. [2025] for latent diffusion models [LDM; Rombach et al., 2022], which perform diffusion within the latent space of a pre-trained encoder-decoder network. Ovanger et al. [2025] extended this work by providing a thorough geostatistical assessment of LDMs against truncated Gaussian random field modeling [Matheron et al., 1987, Mannseth, 2014] for multi-facies scenarios. The authors present overall high modeling performances, but note biases due to the LDM data compression. Diffusion models were also recently introduced to solve inverse modeling problems in the Earth sciences. Wang et al. [2023] used pre-trained DMs as regularizers within a deterministic full waveform inversion (FWI) of seismic data, integrating the FWI's iterative updates with DM sampling. This framework, designed for subsurface wavespeed predictions, was extended to multiple elastic properties by Taufik et al. [2024]. Both studies demonstrate improved accuracy and more realistic results compared to conventional FWI for synthetic geological scenarios. Wang et al. [2024] further proposed a controllable DM-based FWI, where the model learns the relationship between embedded conditioning data and wavespeed distributions. Finally, Di Federico and Durlofsky [2025] show that stochastic inverse modeling can be carried out by combining a pre-trained unconditioned LDM with an ensemble-based inversion method; the authors demonstrated their approach on facies prediction tasks in the context of history matching.

Beyond Earth sciences, the field of inverse modeling with DMs is of broad interest for computer vision and biomedical imaging, and several methodologies were recently proposed; we refer to Daras et al. [2024] and Zhao et al. [2025] for comprehensive overviews. Analogously to methods based on GANs and VAEs, direct training on conditioning data is a popular approach [e.g., Dhariwal and Nichol, 2021, Xu et al., 2024, Aouf et al., 2025, Lee et al., 2025, Wang et al., 2024, Ho and Salimans, 2021, Whang et al., 2022, Liu et al., 2023], but implies computationally demanding re-training when considering new data types or designs. Alternatively, one can rely on inference frameworks that iterate *outside* the generative process of pre-trained unconditional DMs. Conventional sampling algorithms (e.g., MCMC) are often inefficient in this setting, due to the DM's large dimensionality and comparatively long generation times [Zhao et al., 2025]. More efficient variational inference algorithms have been proposed for posterior approximation with surrogate modeling, but they often struggle to capture complex or multimodal posterior distributions [e.g., Mardani et al., 2023, Alkan et al., 2023, Feng and Bouman, 2024]. Ensemble-based approaches [e.g., Di Federico and Durlofsky, 2025] can

be limited by comparatively high computational costs; LDMs can be used to reduce dimensionality, but the associated encoder-decoder networks (e.g., VAE or GAN) introduce additional complications such as reduced modeling ability [e.g., leading to bias or smoothing; Ovanger et al., 2025] and non-linearities [Daras et al., 2024].

Another family of conditioning approaches leverage the sequential nature of the denoising process. For example, SMC can be used to progressively sample, at different denoising steps, a posterior distribution that evolves towards the posterior pdf [e.g., Trippe et al., 2022, Cardoso et al., 2023, Wu et al., 2024, Dou and Song, 2024]. These asymptotically exact methods work under the assumption of infinite sampling and linear physics. As an alternative, the denoising process itself can be adapted to achieve approximate Bayesian posterior sampling at low computational costs [Song et al., 2021b], provided that the intractable likelihood is approximated at each denoising step. The approximated likelihood score is then combined with the pre-trained denoising score to steer the denoising generative process towards posterior samples. Among numerous such approaches [see e.g., Daras et al., 2024], Diffusion Posterior Sampling (DPS) [Chung et al., 2023] has gained wide popularity as it allows inference for both linear and nonlinear inverse problems. Nonetheless, this class of conditional samplers are affected by the likelihood approximation [Daras et al., 2024]. For instance, the accuracy of DPS decreases with the conditioning data noise magnitude and increasing nonlinearity of the problem at hand [Chung et al., 2023]. Various adjustments have been proposed in the implementation of DPS, including ad-hoc weighting of the likelihood score. Several studies have highlighted these limitations and proposed partial improvements for linear inverse problems [e.g., Hamidi and Yang, 2025, Boys et al., 2024, Yismaw et al., 2025, Song et al., 2023].

In this work, we investigate DMs for multivariate subsurface geological modeling and propose improvements to DPS for inversion tasks. Our corrected DPS (CDPS) relies on a likelihood approximation that considers not only the observational error of the conditioning data, but also the impact of the noise contamination at the different stages of the DM. The modified likelihood approximation removes the need to arbitrarily weight the likelihood score and is expected to improve robustness and uncertainty quantification. We further highlight inconsistencies in the original implementation of DPS by Chung et al. [2023] implemented with Denoising Diffusion Probabilistic and Implicit Modeling [DDPM and DDIM; Ho et al., 2020, Song et al., 2021a] and suggest corrections. In our study, we rely on a state-of-the-art DM implementation [EDM; Karras et al., 2022] to model a bivariate prior pdf describing sedimentary channel sequences and correlated acoustic impedances. We first demonstrate substantial increases in prior modeling performance against a GAN and a VAE previously introduced for analogous tasks [Miele et al., 2024]. Then, we use CDPS to condition realizations on both local observations (well logs) and nonlinear geophysical data (fullstack seismic data), considering Gaussian data noise of different magnitudes. We demonstrate that CDPS yields significantly improved accuracy and enhanced robustness compared to DPS across all considered applications, while allowing for a reduction in the required number of denoising steps. Our results for the linear conditioning case compare well with those sampled with the preconditioned Crank–Nicolson (pCN) MCMC algorithm [Cotter et al., 2013]. The CDPS can easily be adapted to different DM formulations and data error levels. We further present the algorithm for DDPM and DDIM, with example applications, in the Appendix.

2 Methodology

2.1 Diffusion modeling

Diffusion models enable deep generative modeling by transforming samples from a tractable distribution (often Gaussian) into samples from an unknown target pdf $p(\mathbf{x}_0)$ on \mathbb{R}^d , from which samples are available (the TI). The diffusion process typically involves corrupting these samples, $\mathbf{x}_0 \sim p(\mathbf{x}_0)$, through the progressive addition of Gaussian noise at different time-steps t , thereby defining the *forward process* $p(\mathbf{x}_t | \mathbf{x}_{t-1})$. After a sufficient time T , the corrupted data distribution $p(\mathbf{x}_T)$ can be considered Gaussian [Ho et al., 2020, Sohl-Dickstein et al., 2015]. The *backward process*, $q(\mathbf{x}_0 | \mathbf{x}_{T:1})$, represents the sampling or generative process, which is analytically intractable for an arbitrary $p(\mathbf{x}_0)$. Numerical methods can be used instead by relying on a trained deep neural network $S_\theta(\cdot)$ [Ho et al., 2020, Sohl-Dickstein et al., 2015].

A generalized continuous-time formulation of diffusion modeling, referred to as *score-based* [e.g., Song et al., 2021b, Song and Ermon, 2019], represents the forward process through stochastic differential equations (SDE) of the form [Song et al., 2021b]

$$d\mathbf{x}_t = f(\mathbf{x}_t, t)dt + g(t)d\mathbf{W}_t, \quad (1)$$

where $f(\mathbf{x}_t, t)$ is a drift term, $g(t)$ is a diffusion coefficient and \mathbf{W}_t is a Wiener process (i.e., Brownian motion). The reverse-time SDE for unconditional sampling is given by [Song et al., 2021b, Anderson, 1982]

$$d\mathbf{x}_t = (f(\mathbf{x}_t, t)dt + g(t)^2 \nabla_{\mathbf{x}_t} \log p_t(\mathbf{x}_t)) dt + g(t)d\mathbf{W}_t, \quad (2)$$

where $\nabla_{\mathbf{x}_t} \log p_t(\mathbf{x}_t)$ is the score function of the noisy data distribution \mathbf{x}_t . The generation of samples using Eq. 2 is possible using Langevin dynamics, implying that a distribution of samples $p(\mathbf{x}_0|\mathbf{x}_T)$ can be obtained from a single \mathbf{x}_T . As an alternative, deterministic sampling can be performed using the ordinary differential equation (ODE) [Song et al., 2021b]

$$\frac{d\mathbf{x}_t}{dt} = \left(f(\mathbf{x}_t, t)dt + \frac{g(t)^2}{2} \nabla_{\mathbf{x}_t} \log p_t(\mathbf{x}_t) \right), \quad (3)$$

which enables a bivariate mapping between \mathbf{x}_T and \mathbf{x}_0 , and is referred to as *probability flow ODE*. The diffusion can be simulated within *Variance preserving* (VP) (i.e., the added noise variance is bounded) or *Variance exploding* (VE) frameworks. For the latter, the forward process (Eq. 1) at a given time-step t can be defined by

$$\mathbf{x}_t = \mathbf{x}_0 + \sigma_t z, \quad z \sim \mathcal{N}(0, I), \quad (4)$$

where σ_t represents the time-dependent noise magnitude. Using Tweedie's formula [Robbins, 1956, Efron, 2011], the score function is

$$\nabla_{\mathbf{x}_t} \log p_t(\mathbf{x}_t) = \frac{\mathbb{E}[\mathbf{x}_0|\mathbf{x}_t] - \mathbf{x}_t}{\sigma_t^2}, \quad (5)$$

where $\mathbb{E}[\mathbf{x}_0|\mathbf{x}_t]$ is a time-dependent conditional expectation of \mathbf{x}_0 given \mathbf{x}_t . Neural networks can be trained to parameterize the score function from noisy data and a given time t , $S_\theta(\mathbf{x}_t, t)$, by minimizing the mean square error [Song et al., 2021b]

$$\mathcal{L}(S_\theta) = \mathbb{E}_{\mathbf{x}_0} \mathbb{E}_{\mathbf{x}_t|\mathbf{x}_0} [||S_\theta(\mathbf{x}_t, t) - \nabla_{\mathbf{x}_t} \log p_t(\mathbf{x}_t|\mathbf{x}_0)||_2^2] \quad (6)$$

or directly as a denoiser $S_\theta(\mathbf{x}_0 + \mathbf{z}, t)$, using [e.g., Karras et al., 2022]

$$\mathcal{L}(S_\theta) = \mathbb{E}_{\mathbf{x}_0} \mathbb{E}_{\mathbf{z} \sim \mathcal{N}(0, \sigma^2 I)} [||S_\theta(\mathbf{x}_0 + \mathbf{z}, t) - \mathbf{x}_0||_2^2]. \quad (7)$$

The trained network is finally used in the backward process (Eq. 2) for generative (prior) modeling.

The original formulations for DMs are the discrete-time DDPM [Ho et al., 2020, Sohl-Dickstein et al., 2015] and its generalization DDIM [Song et al., 2021a]. Here, $S_\theta(\mathbf{x}_t, t)$ is trained to predict the noise in \mathbf{x}_t , $\epsilon_\theta^{(t)}$, and the generative process for both DDPM and DDIM is defined by

$$\mathbf{x}_{t-1} = \sqrt{\bar{\alpha}_{t-1}} \left(\frac{\mathbf{x}_t - \sqrt{1 - \bar{\alpha}_t} \epsilon_\theta^{(t)}}{\sqrt{\bar{\alpha}_t}} \right) + \sqrt{1 - \bar{\alpha}_{t-1} - \tilde{\sigma}_t^2} \epsilon_\theta^{(t)} + \tilde{\sigma}_t \epsilon_t, \quad (8)$$

where β_t defines the noise schedule of the diffusion process, $\alpha_t = 1 - \beta_t$, $\hat{\alpha}_t = \prod_{s=1}^t \alpha_s$ and $\tilde{\sigma}_t^2$ is the conditional variance sequence (injected noise during sampling), and $\epsilon_t \sim \mathcal{N}(0, I)$. DDIM and DDPM are discretizations of score-based diffusion, with $\epsilon^{(t)} = -\nabla_{\mathbf{x}_t} \log p_t(\mathbf{x}_t) \sqrt{1 - \bar{\alpha}_t}$ [Dhariwal and Nichol, 2021, Song et al., 2021b]. In DDPM, $\tilde{\sigma}_t = \sqrt{\frac{1 - \bar{\alpha}_{t-1}}{1 - \bar{\alpha}_t}} \sqrt{\frac{1 - \bar{\alpha}_t}{\bar{\alpha}_{t-1}}}$, while in the DDIM framework $\tilde{\sigma}_t$ is set to 0 for deterministic sampling [Ho et al., 2020, Song et al., 2021b], and can hence be associated to a VP SDE and VP ODE, respectively.

2.2 Diffusion Posterior Sampling (DPS)

In Bayesian inversion, one is interested in characterizing or sampling from the posterior pdf, $p(\mathbf{x}_0|\mathbf{d})$, with the data vector \mathbf{d} given by

$$\mathbf{d} = \mathcal{F}(\mathbf{x}_0) + \epsilon_{\mathbf{d}}, \quad (9)$$

where $\mathcal{F}(\cdot)$ corresponds to a forward operator (either linear or nonlinear) and $\epsilon_{\mathbf{d}}$ is the noise in the observed data. The inversion problem can be formalized by Bayes' theorem, for a constant model dimension, as $p(\mathbf{x}_0|\mathbf{d}) \propto p(\mathbf{d}|\mathbf{x}_0)p(\mathbf{x}_0)$, where $p(\mathbf{d}|\mathbf{x}_0)$ is the likelihood function.

Unconditional modeling from $p(\mathbf{x}_0)$ can be achieved with a trained DM, using Eqs. 2 or 3. Following Bayes' rule, sampling from the posterior pdf can in theory be achieved using the score function [Song et al., 2021b]

$$\nabla_{\mathbf{x}_t} \log p_t(\mathbf{x}_t|\mathbf{d}) = \nabla_{\mathbf{x}_t} \log p_t(\mathbf{x}_t) + \nabla_{\mathbf{x}_t} \log p_t(\mathbf{d}|\mathbf{x}_t), \quad (10)$$

where the first term can be approximated by the trained neural network $S_\theta(\mathbf{x}_t, t)$ and $\nabla_{\mathbf{x}_t} \log p_t(\mathbf{d}|\mathbf{x}_t)$ is a noise-dependent likelihood score. In what follows, we will refer to $\nabla_{\mathbf{x}_t} \log p_t(\mathbf{x}_t)$ as the *prior score*. If $S_\theta(\mathbf{x}_t, t) \simeq$

$\nabla_{\mathbf{x}_t} \log p_t(\mathbf{x}_t)$ (Eq. 6), then $\hat{\mathbf{x}}_0^{(t)}$ is derived using Tweedie's formula (Eq. 5). Otherwise, it is directly obtained as $\hat{\mathbf{x}}_0^{(t)} = S_\theta(\mathbf{x}_t, t)$ (Eq. 7). The likelihood score is given by an intractable integral

$$p_t(\mathbf{d}|\mathbf{x}_t) = \int p(\mathbf{d}|\mathbf{x}_0)p(\mathbf{x}_0|\mathbf{x}_t)d\mathbf{x}_0. \quad (11)$$

Chung et al. [2023] note that for a given \mathbf{x}_t , an estimate of the expected mean for $p(\mathbf{x}_0|\mathbf{x}_t)$ is given by the denoiser $\hat{\mathbf{x}}_0^{(t)} = \mathbb{E}[\mathbf{x}_0|\mathbf{x}_t]$ (Eq. 5); therefore, the likelihood can be approximated as $p(\mathbf{d}|\mathbf{x}_t) \simeq p(\mathbf{d}|\hat{\mathbf{x}}_0^{(t)})$, and

$$\nabla_{\mathbf{x}_t} \log p(\mathbf{d}|\mathbf{x}_t) \simeq \nabla_{\mathbf{x}_t} \log p(\mathbf{d}|\hat{\mathbf{x}}_0^{(t)}). \quad (12)$$

In practice, the score in Eq. 12 is computed by backpropagating the log-likelihood approximations at each time step t . This approach is referred to as Diffusion Posterior Sampling (DPS), and was proposed by Chung et al. [2023] as a general inference framework for both linear and nonlinear inverse problems. Assuming uncorrelated and homoscedastic Gaussian data errors, Chung et al. [2023] use the likelihood

$$p(\mathbf{d}|\hat{\mathbf{x}}_0^{(t)}) = \frac{1}{\sqrt{(2\pi)^n \sigma_{\mathbf{d}}^{2n}}} \exp\left(-\frac{\|\mathcal{F}(\hat{\mathbf{x}}_0^{(t)}) - \mathbf{d}\|_2^2}{2\sigma_{\mathbf{d}}^2}\right), \quad (13)$$

where $\sigma_{\mathbf{d}}$ is the standard deviation of the data noise $\epsilon_{\mathbf{d}}$, leading to

$$\nabla_{\mathbf{x}_t} \log p(\mathbf{d}|\mathbf{x}_t) \simeq \nabla_{\mathbf{x}_t} \log p(\mathbf{d}|\hat{\mathbf{x}}_0^{(t)}) = -\frac{1}{\sigma_{\mathbf{d}}^2} \nabla_{\mathbf{x}_t} \|\mathcal{F}(\hat{\mathbf{x}}_0^{(t)}) - \mathbf{d}\|_2^2. \quad (14)$$

This approximation does not account for errors in the $\hat{\mathbf{x}}_0^{(t)}$ estimate. In their implementation, Chung et al. [2023] propose a weight to the likelihood score, replacing $\frac{1}{\sigma_{\mathbf{d}}^2}$ with a hyperparameter ρ , to account for the impact of errors in the likelihood approximation. In their accompanying code, the authors further replace the sum of square error in Eq. 14 with the root-mean-square error (RMSE), justifying this choice as a solution for increased stability [see open review in Chung et al., 2023]. This arbitrary choice will drastically decrease the magnitude of the likelihood score and, hence, decrease the weight given to the data in the sampling process.

The conditional score approximation used within DPS results in a too low variance of the generated samples; it has been argued that the sampling process is rather associated to the maximization of a posterior than to posterior sampling [Xu et al., 2025]. Improvements to this approximation should include the impact of errors in the denoiser ($\hat{\mathbf{x}}_0^{(t)}$) [Hamidi and Yang, 2025, Boys et al., 2024, Yismaw et al., 2025, Song et al., 2023, Peng et al., 2024]. Following Efron [2011], the denoiser's variance can be computed using Tweedie's formula for the second moment

$$\text{Var}\{\hat{\mathbf{x}}_0^{(t)}|\mathbf{x}_t\} = \sigma_t(1 + \sigma_t \nabla_{\mathbf{x}_t}^2 \log p_t(\mathbf{x}_t)), \quad (15)$$

where $\nabla_{\mathbf{x}_t}^2 \log p_t(\mathbf{x}_t)$ is the Hessian matrix of the score of the data distribution \mathbf{x}_t . Using the Hessian directly is computationally demanding, as its calculation scales exponentially with the model's dimensionality [Boys et al., 2024]. The Covariance-Aware Diffusion Posterior Sampling [Hamidi and Yang, 2025] for linear inversion uses an approximation of the Hessian, computed as the difference between the scores at consecutive and sufficiently small time-steps (i.e., using the finite difference method). The ΠIGDM [Song et al., 2023] and CoDPS [Yismaw et al., 2025] methods use time-step dependent-heuristic approximations of the denoiser's standard deviation for linear inverse problems, representing significantly faster solutions. Peng et al. [2024] derived a formulation to derive the denoiser variance ($\tilde{\sigma}_t$ in Eq. 8) for specific types of DM networks [Dhariwal and Nichol, 2021]. For more general applications, they suggest to estimate the denoiser variance directly from the denoising errors of the trained model, using known test data. In the following, we adopt the latter approach, and introduce a general and consistent formulation for approximate posterior sampling for both linear and nonlinear conditioning data.

2.2.1 Corrected Diffusion Posterior Sampling (CDPS)

The proposed corrected DPS (CDPS), in which the likelihood formulation accounts for the denoising-step-dependent error $\epsilon_{\hat{\mathbf{x}}_0}^{(t)}$ of the trained model. The $\epsilon_{\hat{\mathbf{x}}_0}^{(t)}$ is the largest at early steps of the backward process and decreases with decreasing σ_t . The forward problem at time t can be written as (c.f., Eq. 9).

$$\mathbf{d} = \mathcal{F}(\hat{\mathbf{x}}_0^{(t)} + \epsilon_{\hat{\mathbf{x}}_0}^{(t)}) + \epsilon_{\mathbf{d}} \quad (16)$$

Assuming an ideal denoiser, we assume $\epsilon_{\hat{\mathbf{x}}_0}^{(t)}$ to be spatially uncorrelated and Gaussian-distributed [Yismaw et al., 2025, Song et al., 2023, Peng et al., 2024]. After training, we evaluate the standard deviation of the error for each data dimension (i.e., cells or pixels), using different test data samples i corrupted with known noise, as $\sigma_{\hat{\mathbf{x}}_0, i}^{(t)} \simeq \sqrt{\sum_{i=1}^N (\hat{\mathbf{x}}_{0, i}^{(t)} - x_{0, i})^2 / N}$. The error distribution depends on the spatial features of the input data, which is computable only through Hessian estimation [Hamidi and Yang, 2025, Boys et al., 2024, Efron, 2011] or using a network predicting conditional covariance [Peng et al., 2024, see Section 2.2]. We assume error homoscedasticity, using the mean value of $\sigma_{\hat{\mathbf{x}}_0}^{(t)}$ from all the pixels.

In agreement with Linde et al. [2017] and Friedli and Linde [2024] who studied approximations to intractable likelihoods arising in geophysics, we propagate the errors, $\sigma_{\hat{\mathbf{x}}_0, i}^{(t)}$, through the forward model using a first-order Taylor expansion $\mathbf{x} \mapsto \mathcal{F}(\mathbf{x})$ around $\hat{\mathbf{x}}_0^{(t)}$,

$$\mathbf{d} \approx \mathcal{F}(\hat{\mathbf{x}}_0^{(t)}) + \mathcal{J}_{\hat{\mathbf{x}}_0^{(t)}} \epsilon_{\hat{\mathbf{x}}_0}^{(t)} + \epsilon_{\mathbf{d}}, \quad (17)$$

where $\mathcal{J}_{\hat{\mathbf{x}}_0^{(t)}}$ is the corresponding Jacobian matrix of the forward operator. Assuming Gaussian distributions $p(\epsilon_{\hat{\mathbf{x}}_0}^{(t)}) = \mathcal{N}(0, \sigma_{\hat{\mathbf{x}}_0}^{2(t)} \mathbf{I}) = \mathcal{N}(0, \Sigma_{\hat{\mathbf{x}}_0}^{(t)})$ and $p(\epsilon_{\mathbf{d}}) = \mathcal{N}(0, \sigma_{\mathbf{d}}^2 \mathbf{I}) = \mathcal{N}(0, \Sigma_{\mathbf{d}})$, the likelihood $p(\mathbf{d}|\hat{\mathbf{x}}_0^{(t)})$ can be approximated as

$$p(\mathbf{d}|\mathbf{x}_t) \simeq p(\mathbf{d}|\hat{\mathbf{x}}_0^{(t)}) = \mathcal{N}(0, \tilde{\Sigma}_{\mathbf{d}}^{(t)}), \quad (18)$$

where $\tilde{\Sigma}_{\mathbf{d}}^{(t)} = \mathcal{J}_{\hat{\mathbf{x}}_0^{(t)}}^T \Sigma_{\hat{\mathbf{x}}_0}^{(t)} \mathcal{J}_{\hat{\mathbf{x}}_0^{(t)}} + \Sigma_{\mathbf{d}}$ (see Friedli and Linde [2024] for further details). For a linear operator (e.g., local conditioning), the full covariance matrix in Eq. 18 is obtained without any approximations, using matrix multiplication with the linear operator. Finally, we re-write the likelihood score (Eq. 14) as

$$\nabla_{\mathbf{x}_t} \log p(\mathbf{d}|\mathbf{x}_t) \simeq \nabla_{\mathbf{x}_t} \log p(\mathbf{d}|\hat{\mathbf{x}}_0^{(t)}) = -\nabla_{\mathbf{x}_t} \left[(\mathcal{F}(\hat{\mathbf{x}}_0^{(t)}) - \mathbf{d})^T \tilde{\Sigma}_{\mathbf{d}}^{-1(t)} (\mathcal{F}(\hat{\mathbf{x}}_0^{(t)}) - \mathbf{d}) \right]. \quad (19)$$

This is the main adaptation introduced by CDPS.

We report on another error in the original DPS implementation on DDPM [Chung et al., 2023]. At each step, the authors use the likelihood score to obtain the conditional denoised image as $\mathbf{x}_{t-1} = \mathbf{x}'_{t-1} - \rho \nabla_{\mathbf{x}_t} \log p(\mathbf{d}|\hat{\mathbf{x}}_0^{(t)})$, where \mathbf{x}'_{t-1} is the denoised image considering the prior score, obtained with Eq. 8 as is. However, this is inconsistent with Bayes' theorem [e.g., Eq. 10; Song et al., 2021b], according to which Eq. 8 in the conditioning case should be

$$\mathbf{x}_{t-1} = \sqrt{\bar{\alpha}_{t-1}} \left(\frac{\mathbf{x}_t - \sqrt{1 - \bar{\alpha}_t} \hat{\epsilon}_{\theta}^{(t)}}{\sqrt{\bar{\alpha}_t}} \right) + \sqrt{1 - \bar{\alpha}_{t-1} - \sigma_t^2} \hat{\epsilon}_{\theta}^{(t)} + \sigma_t \epsilon_t. \quad (20)$$

where $\hat{\epsilon}_{\theta}^{(t)} = \epsilon_{\theta}^{(t)} - \sqrt{1 - \bar{\alpha}_t} \nabla_{\mathbf{x}_t} \log p(\mathbf{d}|\hat{\mathbf{x}}_0^{(t)})$, following the guided diffusion modeling approach proposed by Dhariwal and Nichol [2021]. In practice, even if one does not consider the error in $\hat{\mathbf{x}}_0^{(t)}$, the likelihood score $\nabla_{\mathbf{x}_t} \log p(\mathbf{d}|\hat{\mathbf{x}}_0^{(t)})$ should be rescaled to the diffusion noise magnitudes rather than to a fixed arbitrary ρ . We suggest that this error may be an additional cause of instability of the DPS method; we provide an implementation of the CDPS for DDPM and DDIM in Appendix C, implementing this correction. The CDPS algorithm for score-based diffusion is given in Algorithm 1, specifically within the EDM diffusion framework [Karras et al., 2022]. Further details on EDM are provided in Section 2.3.

2.3 Multivariate diffusion modeling

The simultaneous sampling of multivariate subsurface properties is carried out within a single generative process. We do not consider formulations involving dimensionality reduction with LDMs [Rombach et al., 2022]. We adopt a VE score-based DM framework, often referred to as EDM [Karras et al., 2022], and use its probability flow ODE for unconditional modeling [Karras et al., 2022]:

$$d\mathbf{x} = -\frac{\sigma_t}{dt} \sigma_t \nabla_{\mathbf{x}_t} \log p_t(\mathbf{x}_t). \quad (21)$$

For posterior sampling (Eq. 10), we substitute the score with $\nabla_{\mathbf{x}_t} \log p_t(\mathbf{x}_t|\mathbf{d})$ using our proposed likelihood approximation (Eq. 19). Sampling is performed by evaluating the ODE at noise levels given by the schedule [Karras et al., 2022]

$$\sigma_{i>0} = \left(\sigma_{max}^{1/\rho} + \frac{i}{N-1} (\sigma_{min}^{1/\rho} - \sigma_{max}^{1/\rho}) \right)^{\rho} \quad \text{and} \quad \sigma_N = 0, \quad (22)$$

Algorithm 1 Corrected DPS (CDPS) algorithm within the EDM diffusion modeling framework by Karras et al. [2022]

1: **Require:** trained network $S_\theta(\cdot)$, conditioning data \mathbf{d} , forward operator \mathcal{F} , maximum number of time steps N , noise schedule σ_i , limits σ_{max} and σ_{min}

2: **for** $\sigma_t = 0, \dots, \sigma_{max}$ **do**
3: **sample** $\mathbf{x}_0 \sim q_{data}$
4: $\mathbf{x}_t \leftarrow \mathbf{x}_0 + \sigma_t \mathbf{z}, \mathbf{z} \sim \mathcal{N}(0, I)$
5: $\hat{\mathbf{x}}_0^{(t)} \leftarrow S_\theta(\mathbf{x}_t, t)$
6: $\sigma_{\hat{\mathbf{x}}_0}^{(t)} \leftarrow \mathbb{E} \left[\sqrt{\sum_{i=1}^N (\hat{x}_{0,i}^{(t)} - x_{0,i})^2 / N} \right]$
7: **end for**

8: **sample** $\mathbf{x}_T \sim \mathcal{N}(0, I)$
9: **for** $i = 0, \dots, N$ **do**
10: $\sigma_t \leftarrow \sigma_i$
11: $\hat{\mathbf{x}}_0^{(t)} \leftarrow S_\theta(\mathbf{x}_t, \sigma_t)$
12: $\nabla_{x_t} \log p_t(\mathbf{x}_t) \leftarrow (S_\theta(\mathbf{x}_t, \sigma_t) - \mathbf{x}_t) / \sigma_t^2$
13: $\Sigma_{\hat{\mathbf{x}}_0}^{(t)} \leftarrow \sigma_{\hat{\mathbf{x}}_0}^{2(t)}$
14: **if** \mathcal{F} is nonlinear **then**
15: $\mathcal{J}_{\hat{\mathbf{x}}_0} \leftarrow \mathcal{J}_{\mathcal{F}}(\hat{\mathbf{x}}_0^{(t)})$
16: $\tilde{\Sigma}_{\mathbf{d}} \leftarrow \mathcal{J}_{\hat{\mathbf{x}}_0^{(t)}}^T \Sigma_{\hat{\mathbf{x}}_0}^{(t)} \mathcal{J}_{\hat{\mathbf{x}}_0^{(t)}} + \Sigma_{\mathbf{d}}$
17: **else**
18: $\tilde{\Sigma}_{\mathbf{d}} \leftarrow \mathcal{F}^T \Sigma_{\hat{\mathbf{x}}_0}^{(t)} \mathcal{F} + \Sigma_{\mathbf{d}}$
19: **end if**
20: $\nabla_{x_t} \log p_t(\mathbf{d} | \hat{\mathbf{x}}_0^{(t)}) \leftarrow -\nabla_{\mathbf{x}_t} \left[(\mathcal{F}(\hat{\mathbf{x}}_0^{(t)}) - \mathbf{d})^T \tilde{\Sigma}_{\mathbf{d}}^{-1} (\mathcal{F}(\hat{\mathbf{x}}_0^{(t)}) - \mathbf{d}) \right]$
21: $\nabla_{x_t} \log p_t(\hat{\mathbf{x}}_0^{(t)} | \mathbf{d}) \leftarrow \nabla_{x_t} \log p_t(\mathbf{d} | \hat{\mathbf{x}}_0^{(t)}) + \nabla_{x_t} \log p_t(\mathbf{x}_t)$
22: $x_{t-1} \leftarrow x_t + (\sigma_t - \sigma_{t-1}) \nabla_{x_t} \log p_t(\hat{\mathbf{x}}_0^{(t)} | \mathbf{d})$
23: **if** $\sigma_{\mathbf{x}}(t) \neq 0$ **then**
24: $\nabla_{x_t} \log p_t(\mathbf{d} | \hat{\mathbf{x}}_0^{(t)})' \leftarrow -\nabla_{\mathbf{x}_t} \left[(\mathcal{F}(\hat{\mathbf{x}}_0^{(t)}) - \mathbf{d})^T \tilde{\Sigma}_{\mathbf{d}}^{-1} (\mathcal{F}(\hat{\mathbf{x}}_0^{(t)}) - \mathbf{d}) \right]$
25: $\nabla_{x_t} \log p_t(\hat{\mathbf{x}}_0^{(t)} | \mathbf{d})' = \nabla_{x_t} \log p_t(\mathbf{d} | \hat{\mathbf{x}}_0^{(t)}) + \nabla_{x_t} \log p_t(\mathbf{x}_t)$
26: $x_{t-1} \leftarrow x_t + (\sigma_t - \sigma_{t-1}) (\frac{1}{2} \nabla_{x_t} \log p_t(\hat{\mathbf{x}}_0^{(t)} | \mathbf{d}) + \frac{1}{2} \nabla_{x_t} \log p_t(\hat{\mathbf{x}}_0^{(t)} | \mathbf{d})')$
27: **end if**
28: **end for**
29: **Output:** $\tilde{\mathbf{x}}_0 \sim p(\mathbf{x}_0 | \mathbf{d})$

where σ_{max} and σ_{min} are the maximum and minimum noise levels in the corrupted data, i is the step number, $i \in \{1, \dots, N\}$, and ρ is an exponential factor. In agreement with the authors' original choices, we found that $\sigma_{max} = 80$, $\sigma_{min} = 0.002$ and $\rho = 7$ provided the best performance. The motivation behind these parameter choices is explained by Karras et al. [2022]. The ODE is evaluated using the Heun's 2nd order method [Ascher and Petzold, 1998] (lines 23-36 in Algorithm 1).

The network $S_\theta(\mathbf{x}_t, t)$ is trained as a denoiser, using an improved training algorithm with noise-specific weights integrated in Eq. 7 as proposed by Karras et al. [2022]. The network architecture relies on the encoder-decoder structure of a U-Net [Ronneberger et al., 2015], as implemented by Dhariwal and Nichol [2021] for general image generation. We use a multi-head self-attention mechanism [Vaswani et al., 2017] at each of its three layers to capture global dependencies. In our implementation, each subsurface property type is represented by a separate channel. Categorical variables such as geological facies assume a single numerical variable within a single dimension. Similarly to Miele et al. [2024] and Miele and Azevedo [2024], the multivariate prior distribution $p(\mathbf{x}_0)$ is represented by a training dataset where each sample is a joint realization of two or more co-located subsurface properties. The data can be represented as a single large image (randomly sampled during training) [see, e.g., Laloy et al., 2018] or as separate samples.

2.4 Performance assessment

Prior modeling performance is assessed by comparing the unconditional subsurface realizations against the TI and realizations generated with two benchmark models, a GAN and a VAE, proposed by Miele et al. [2024] for an analogous case study. The statistical distance between the target and modeled distributions (either prior or posterior) were quantified using the root-mean-square-error (RMSE) and the Kullback-Leibler divergence (KL) [Kullback and Leibler, 1951]. The similarity of spatial features in the realizations was assessed using the structural similarity index (SSIM) [Wang et al., 2004] defined as

$$\text{SSIM}(\mathbf{u}, \mathbf{v}) = \frac{(2\mu_{\mathbf{u}}\mu_{\mathbf{v}} + C_1)(2\sigma_{\mathbf{u}\mathbf{v}} + C_2)}{(\mu_{\mathbf{u}}^2 + \mu_{\mathbf{v}}^2 + C_1)(\sigma_{\mathbf{u}}^2 + \sigma_{\mathbf{v}}^2 + C_2)}, \quad (23)$$

where \mathbf{u} and \mathbf{v} define sliding windows of size $M \times M$, on two different images, μ and σ are their corresponding mean and standard deviations, and C is a constant. Following the original implementation [Wang et al., 2004] and previous related works [e.g., Levy et al., 2023, Miele et al., 2024], we set $M = 7$, $C_1 = 0.01$ and $C_2 = 0.03$. The SSIM ranges between -1 and 1, with 1 indicating a perfect match between images. Further metrics concerning the reproduction of facies volume fractions, two-points statistics (i.e., variograms), and lateral continuity (shape) of geological features, are presented in Appendix A.

Convergence of the inversions results was assessed using the weighted RMSE (WRMSE), a data misfit weighted by the data standard deviation $\sigma_{\mathbf{d}}$, defined as

$$\text{WRMSE} = \sqrt{\frac{1}{N_{\mathbf{d}}} \sum \left[\frac{\mathbf{d}_i - \mathcal{F}(\mathbf{x}_0)_i}{\sigma_{\mathbf{d},i}} \right]^2}. \quad (24)$$

A $\text{WRMSE} \leq 1.1$ is chosen to indicate convergence in terms of data misfit as the residuals have a similar statistic as the observational noise and a $\text{WRMSE} < 1$ may indicate overfitting of the noisy data. Moreover, the predictive power of the inferred pdf is assessed using the logarithmic scoring rule (logS) [Good, 1952], computed as $\text{logS}(\hat{p}, \mathbf{d}) = -\log \hat{p}(\mathbf{d})$, where \hat{p} is the inferred pdf and \mathbf{d} is the real data. A lower value of logS corresponds to a better approximation. The proposed CDPS is compared to the original DPS [Chung et al., 2023] and to a sampling method based on Markov chain Monte Carlo (MCMC). For MCMC, we use the preconditioned Crank–Nicolson algorithm (pCN) [Cotter et al., 2013], which is well-suited for high-dimensional problems. In this method, each new proposal \mathbf{x}_{new} is defined by $\mathbf{x}_{new} = \sqrt{1 - \beta^2} \mathbf{x}_{old} + \beta \mathbf{z}$, where \mathbf{x}_{old} represents the previous state, β is a constant determining the step size, $\mathbf{z} \sim \mathcal{N}(0, \mathbf{C})$, and \mathbf{C} is the prior covariance, determining the jump rate. The acceptance probability α takes the form $\alpha(\mathbf{x}_{new}, \mathbf{x}_{old}) = \min(1, (p(\mathbf{d}|\mathbf{x}_{new})/p(\mathbf{d}|\mathbf{x}_{old})))$. Convergence of the pCN samples is determined with the Gelman-Rubin diagnostic [Gelman and Rubin, 1992] using $\hat{R} \leq 1.2$ for all model parameters as a criterion. We further assess the exploration of the parameter space by computing within-chain autocorrelation of samples, that is measuring the covariance between two samples divided by the parameter's variance.

2.5 Code implementation

The methods were implemented in Python (Python 3.12) using PyTorch (PyTorch 2.5) libraries with CUDA implementation. The training of all the generative models and the corresponding unconditional and conditional modeling were performed using a single GPU NVIDIA™ GeForce® GTX TITAN X (CUDA 12.2). The pCN sampling was performed on the same machine, generating DM samples using this GPU. No parallelization on different GPUs was considered. Training, modeling and sampling times mentioned in Section 3.3 are specific to this machine.

3 Results

We evaluate the generative performance of the trained DM by parameterizing a bivariate prior pdf, describing a sequence of lenticular sandy channels in a shale background (facies), and the associated acoustic impedances (I_P). We consider an area of 100×80 cells, assumed to have sides of 1 m (Fig. 1). The TI consists of 3000 samples (Fig. 1a) of MPS facies realizations, generated using Petrel software (SLB) based on a 3D conceptual geological model. Shales and sands are categorized as 0 and 1, respectively. The facies distribution ensemble is spatially uniform, with each cell having average $p(\text{sand}) = 0.3$ (Fig. 1c). The facies-dependent I_P is represented using direct sequential co-simulations with multi-local distribution functions [Nunes et al., 2017, Soares, 2001]. We account for facies-dependent I_P marginal distributions (Fig. 1b) and spatial models (2D variograms; detailed in Appendix A). The average spatial distribution of I_P (Fig. 1d) is primarily dependent on facies with an area of relatively lower values in the lower-right section of the considered area. The DM was trained for a total of 600 epochs (225000 steps). The GAN and VAE used for benchmarking were trained on the same TI, for a total of 2000 epochs, using the hyperparameters proposed by Miele et al. [2024].

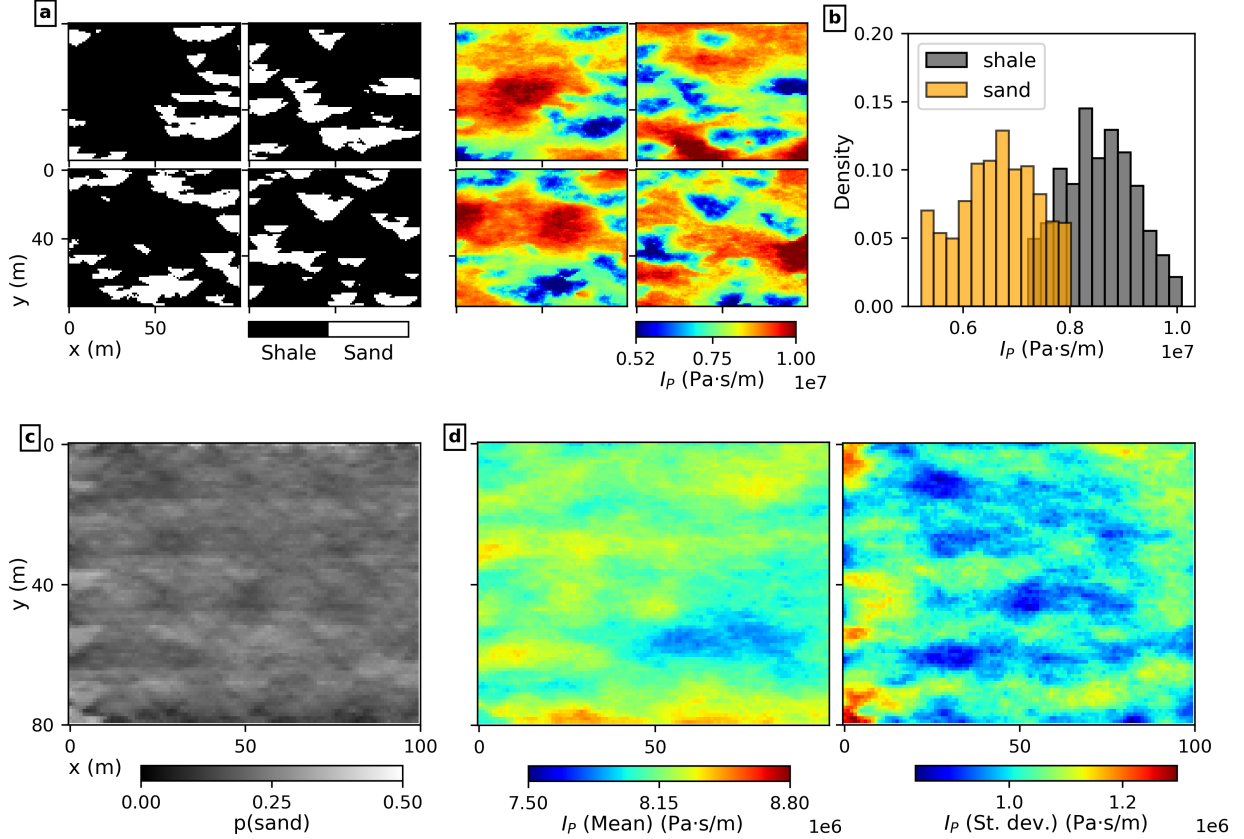


Figure 1: Prior distribution as represented in the training dataset: (a) Facies and I_P realizations; (b) I_P distribution per facies; (c) probability of sand distribution; (d) point-wise average and standard deviation of I_P .

3.1 Unconditional modeling

Prior modeling performances are assessed on 1000 unconditional samples generated from the trained DM, GAN and VAE each. The channel morphologies and I_P spatial patterns reproduced by DM and GAN (*Samples* in Fig. 2a and c) are visually indistinguishable from those of the TI (Fig. 1a). For DM, the $p(\text{sand})$ and average I_P match the prior accurately; Table 1 shows the average relative error for the two property types. Of the two benchmarking models, the GAN's $p(\text{sand})$ and average I_P distributions (Fig. 2c) show significant deviations from the prior. In fact, the overestimation of $p(\text{sand})$ in the central area may indicate mode collapse. Despite the smooth spatial features in the generated samples (Fig. 2e), the VAE performs better than GAN at capturing both properties average distributions, and displays even a larger accuracy than DM for facies (Table 1).

The joint distributions of facies and co-located I_P obtained from the sampled realizations (Fig. 2b, d, and f) show significantly superior modeling ability of the DM (Fig. 2b). The facies classes are modeled with negligible errors (i.e., facies values different from 0 and 1); the corresponding I_P marginal distributions (plotted along the y-axes) match accurately the prior means and standard deviations, fitting the data with a KL divergence approximately five times lower than for GAN and VAE (Table 1). Further analysis of the networks unconditional modeling performances focusing on geostatistical metrics, are provided in Appendix A.

3.2 Inverse modeling using CDPS

We evaluated the proposed CDPS by considering both linear and nonlinear inverse problems using a test realization from the prior distribution as our "True" facies and I_P (Fig. 3a). The linear test case consists in generating samples that are locally conditioned on direct observations. The data, \mathbf{d}_{obs} , are obtained from two wells ("Well 1" and "Well 2" in Figure 3a). This problem is analogous to an *image inpainting* task in computer vision, where missing parts of

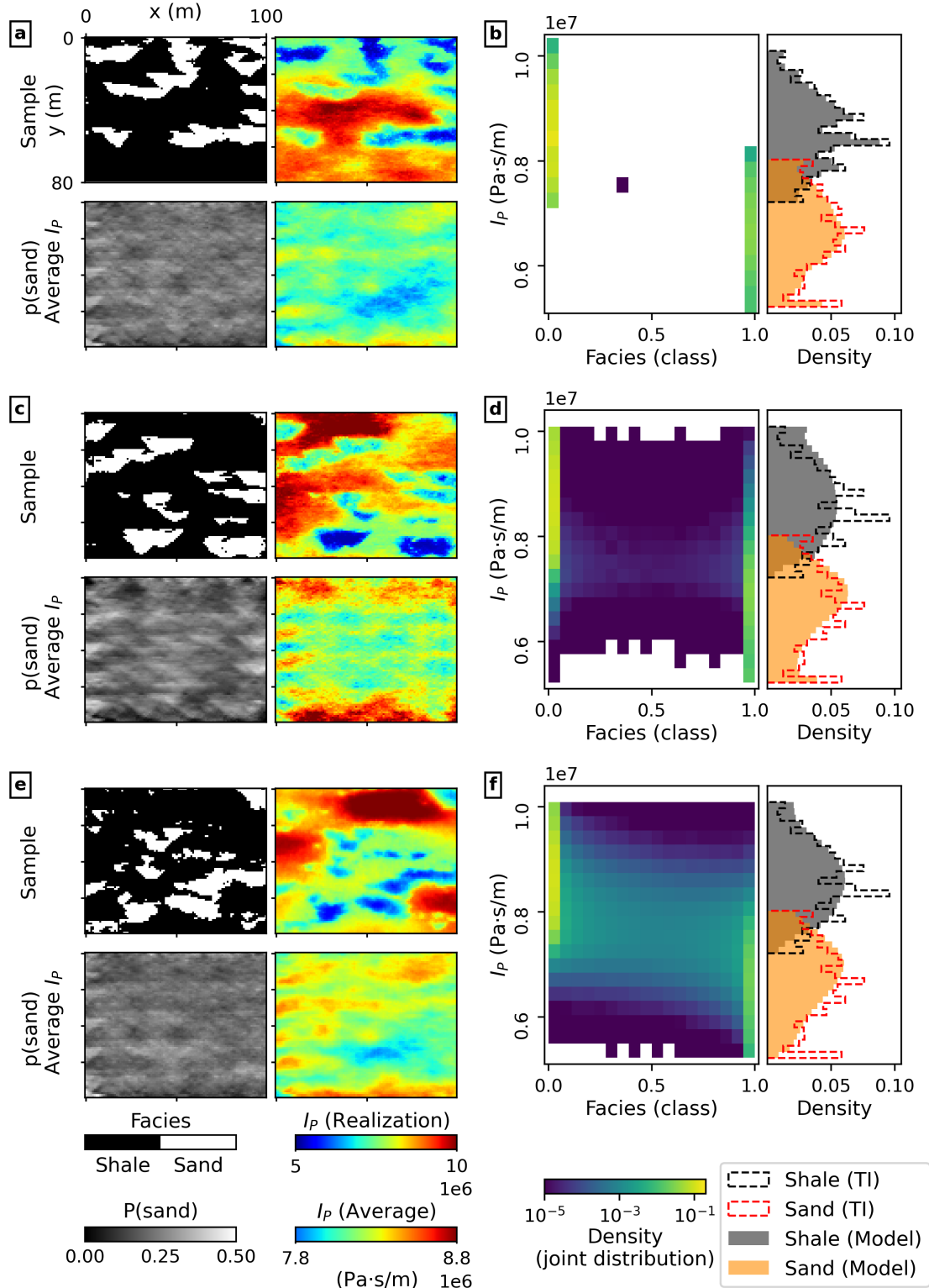


Figure 2: Summary of unconditional modeling performances of (a, b) DM, (c, d) GAN, and (e, f) VAE. Subplots (a), (c), (e): realizations and average distribution of facies and I_P for (a) DM, (c) GAN and (e) VAE; subplots (b), (d), (f): joint and I_P distributions for (b) DM, (d) GAN and (f) VAE.

Table 1: Metrics for unconditional prior modeling using the trained DM and benchmarking GAN and VAE. The $p(\text{sand})$ and Avg. I_P refer to the average models obtained from the realizations ensembles, shown in Figure 2a, c, e. KL : Kullback–Leibler divergence; Avg.: average; St. dev.: standard deviation.

	Lithology	$p(\text{sand})$ — Avg. I_P	I_P marginal distributions	
		Relative error	Avg. \pm St. dev. ($10^6 \text{ Pa} \cdot \text{s/m}$)	KL_{I_P} (10^{-3})
Prior	<i>Sand</i>	-	6.66 ± 0.73	-
	<i>Shale</i>		8.54 ± 0.66	-
DM	<i>Sand</i>	8.3%	6.65 ± 0.73	0.25
	<i>Shale</i>	0.8%	8.53 ± 0.68	0.42
GAN	<i>Sand</i>	21.0%	6.75 ± 0.77	2.1
	<i>Shale</i>	2.1%	8.70 ± 0.72	1.1
VAE	<i>Sand</i>	7.0%	6.87 ± 0.76	1.3
	<i>Shale</i>	1.2%	8.62 ± 0.69	1.5

Table 2: Noise contamination levels of the conditioning data (\mathbf{d}_{obs}) for the linear and nonlinear inversion examples.

	Linear $\sigma_{F_{\text{ac.}}}, \sigma_{I_P}$ ($10^6 \text{ Pa} \cdot \text{s/m}$)	Nonlinear r, σ_c (Amplitude)
Data noise 1	0.05, 0.12	0.025, 0.5
Data noise 2	0.1, 0.23	0.05, 1
Data noise 3	0.2, 0.5	0.1, 2

images are generated conditioned on the known regions. The nonlinear example is a geophysical inversion problem with fullstack seismic data (Fig. 3c), assumed to be derived from the true I_P , and modeled as follows. First, vertical sequences of impedance contrasts (R) are computed following $R_i = (I_{P_{i+1}} - I_{P_i})/(I_{P_{i+1}} + I_{P_i})$, where the subscript i indicates an I_P sample. Then, each trace is convolved with a known seismic source wavelet; in our case, a Ricker wavelet with central frequency of 25Hz and resolution of 3 ms. For both case studies, we evaluated the CDPS under different Gaussian data noise conditions (Table 2).

We compare the results to those obtained with DPS [Chung et al., 2023]. For fair comparison of the two theoretical approaches, we implemented the DPS within the EDM framework used in this work: following DPS theory, we compute the actual Gaussian log-likelihood considering \mathbf{d}_{obs} noise only (e.g., Eq. 14 for absolute $\sigma_{\mathbf{d}}$) and sum it to the prior score for denoising (i.e., Algorithm 1 without lines 13-19).

Using 300 validation examples from the TI we evaluated the modeling error $\sigma_{\hat{\mathbf{x}}_0}^{(t)}$ for 1000 denoising steps. Examples of pixel-dependent uncertainties are shown in Fig. 4a, while the full homoscedastic noise sequence used is shown in Fig. 4b. Here, even if the facies classes are categorical, they are modeled as a continuous variable by DM and treated as such in the likelihood score computation. In Appendix B, we present applications of CDPS using well and seismic data simultaneously.

3.2.1 Linear conditioning results

For the linear conditioning case, we considered three test cases involving the contamination of \mathbf{d}_{obs} (Figure 3b) with different levels of uncorrelated Gaussian noise ($\sigma_{F_{\text{ac.}}}$ and σ_{I_P} , see Table 2). Figure 5a shows the score magnitudes, expressed as L2-norms, for CDPS and DPS as a function of denoising/generative steps. For all settings, the scores of the data distribution have very similar values and decreasing trends; an average for the three noise levels is plotted as dashed lines. The likelihood scores show generally an inverse correlation between their magnitude and the data noise level, highlighting a stronger constraining effect of low-noise \mathbf{d}_{obs} . This correlation is negligible for the CDPS after 300 diffusion steps, with $\nabla_{\mathbf{x}_t} \log p_t(\mathbf{d}|\mathbf{x}_t)$ being approximately 30 times lower than $\nabla_{\mathbf{x}_t} \log p_t(\mathbf{x}_t)$. A similar trend is observed in DPS only for the the largest data noise case (*Data noise 3*), while the likelihood score values generally increase with decreasing data error.

For each scenario, we generated 100 conditional samples. The convergence of the CDPS process is shown in Figure 5d as the WRMSE between the predicted $\hat{\mathbf{x}}_0^{(t)}$ ($\hat{\mathbf{x}}_0^{(t)} = \mathbf{x}_0$ at $t = 0$) and \mathbf{d}_{obs} . Between 93 and 95% of the generated CDPS samples converged to a WRMSE < 1.1 . For DPS, none of the samples converged when considering the lowest noise levels, and 99% of the samples converged to a WRMSE < 1.1 for the two larger-error cases. Overall, the WRMSE of the DPS samples approach lower values faster than CDPS during the denoising process; for *Data noise 1*, the DPS

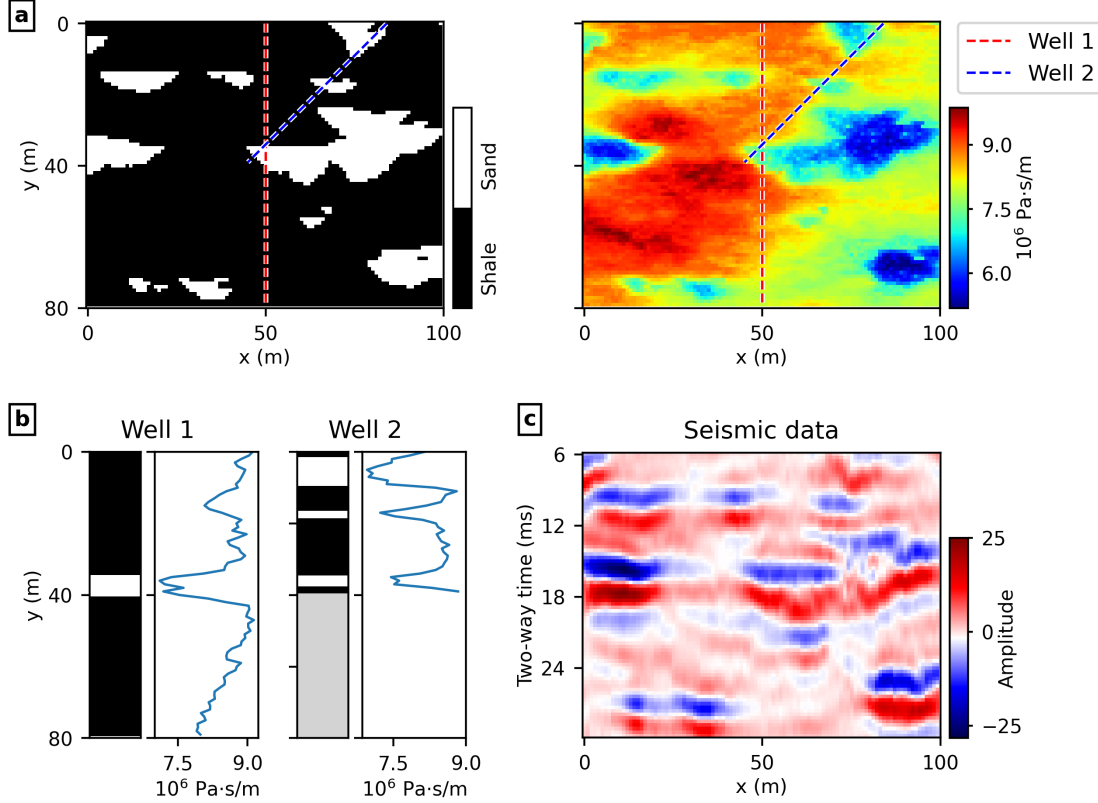


Figure 3: Test model used in inverse modeling: (a) real subsurface distribution ("True") and location of the two wells used for the linear inversion; (b) conditioning well log data for the linear inversion; (c) conditioning seismic data for the nonlinear inversion.

samples ($\hat{\mathbf{x}}_0^{(t)}$) initially overfit the data noise ($\text{WRMSE} < 1$) before diverging ($\text{WRMSE} \approx 1.5$). The WRMSE values obtained by CDPS also show comparatively larger variance (i.e., DPS samples follow similar paths).

Figures 6a and b show the ensembles of realizations sampled by CDPS and DPS, respectively, for the *Data noise 2* case. The realizations generally converge correctly at well locations, and show increasingly larger variability with an increasing distance from the wells, approaching the prior model. Considering, as example, the unconditioned leftmost area between $x = 0 \text{ m}$ and $x = 20 \text{ m}$, CDPS better represents this uniformity, with $p(\text{sand}) = 0.36$ and $I_P = (7.40 \pm 1.08) \times 10^6 \text{ Pa} \cdot \text{s/m}$, while DPS shows non-uniform channel distributions, with $p(\text{sand}) = 0.50$ and $I_P = (7.12 \pm 0.88) \times 10^6 \text{ Pa} \cdot \text{s/m}$. We further attempted to sample the posterior using pCN MCMC, considering $\beta = 0.03$ and three independent chains, for 50000 iterations. After a burn-in time of 25000 iterations, only 60 parameters of the 120 conditioned parameters satisfied the \hat{R} statistics threshold of 1.2. The ensemble of the sampled solutions are shown in Fig. 6c. Here, local conditioning is effective, but large variance (particularly evident in the facies distribution) highlight the points of non-convergence of the pCN. The unconditioned area between $x = 0 \text{ m}$ and $x = 20 \text{ m}$ has $p(\text{sand}) = 0.28$ and $I_P = (7.90 \pm 1.03) \times 10^6 \text{ Pa} \cdot \text{s/m}$ and shows facies and I_P spatial patterns closer to those of the CDPS. However, the samples show poor mixing: on average, the converged parameters show autocorrelation values lower than 0.2 only after 400 samples (i.e., each chain has approximately 62 independent samples).

Figure 7 shows the realizations of I_P sampled by the three methods at the well locations, while their agreement with the target data (\mathbf{d}_{obs} without noise) is summarized in Table 3. The DPS results present a comparatively poorer fit to the data than CDPS (Fig. 7b), showing larger WRMSE and logS values than for CDPS. While the pCN results fit the data within the noise assumptions (Fig. 7c), it shows relatively larger logS and RMSE values than CDPS to Well 2 data. These discrepancies may be due to the lack of sufficient posterior samples as indicated by the limited convergence of the MCMC chains.

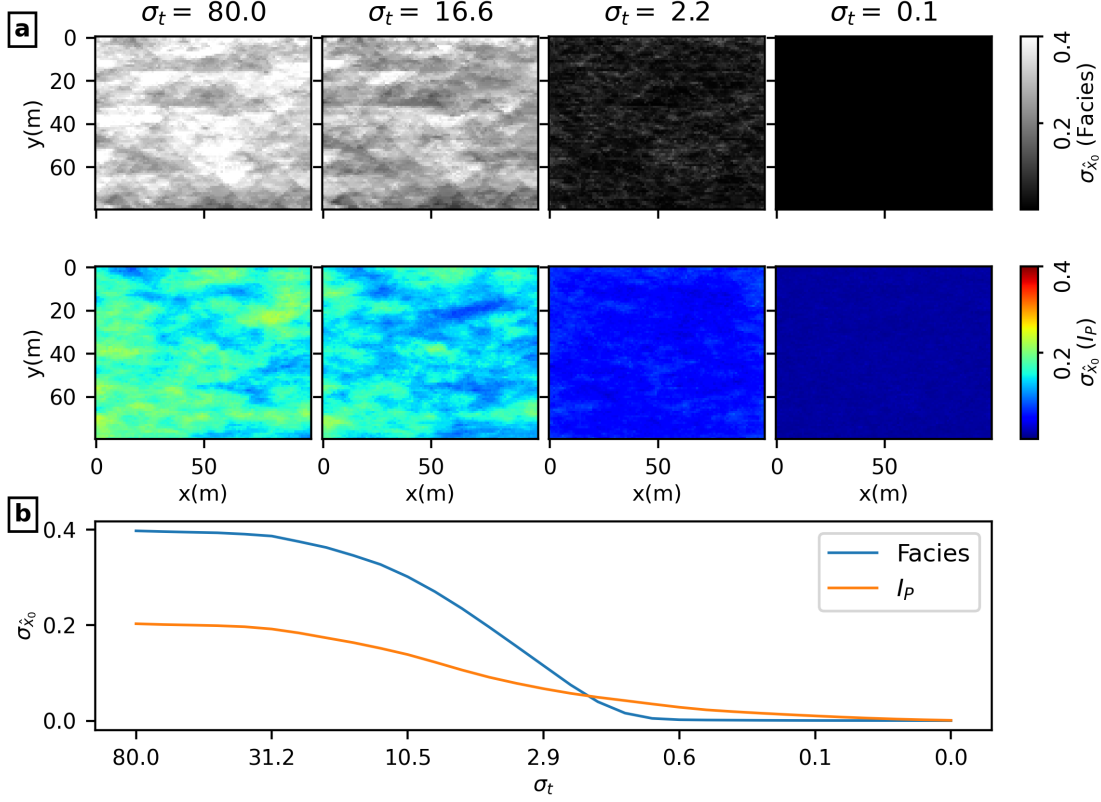


Figure 4: Modeling error: (a) examples of errors at specific noise levels; (b) standard deviation of the homoscedastic error considered. The values refer to the raw network output, of range $[0, 1]$.

Table 3: RMSE and logS measures of the predicted I_P for the linear inversion, considering the *Data noise 2* case.

	Well 1			Well 2		
	CDPS	DPS	pCN	CDPS	DPS	pCN
WRMSE	0.70	0.74	0.72	0.79	0.78	0.86
LogS	13.2	14.0	13.2	13.3	13.6	13.7
LogS (Prior)	15.9			15.7		

3.2.2 Nonlinear inversion results

We ran the nonlinear inversion example for three noise-levels in \mathbf{d}_{obs} (Fig. 3c), considering absolute and relative components of the standard deviations (σ_c and r , respectively, in Table 2). Similar to the linear case, the prior scores (Fig. 5b) display a decreasing trend that does not change significantly for different noise levels. The $\nabla_{\mathbf{x}_t} \log p_t(\mathbf{d}|\mathbf{x}_t)$ values of CDPS show a similar decreasing trend for the three noise levels, ranging from one-tenth to similar values as $\nabla_{\mathbf{x}_t} \log p_t(\mathbf{x}_t)$. Unlike the linear case, these scores show persistent differences between noise scales, with a maximum difference of one order of magnitude between the minimum and maximum data noise used. For DPS, the $\nabla_{\mathbf{x}_t} \log p_t(\mathbf{d}|\mathbf{x}_t)$ values are comparatively larger than CDPS and rapidly exceed the prior scores, becoming up to ten times larger (*Data noise 1*).

All samples obtained with CDPS converged to a $\text{WRMSE} < 1.1$ (Fig. 5e). On the other hand, convergence of the DPS samples occurred only for the larger data noise case, while none of the samples converged for *Data noise 1* ($\text{WRMSE} = 1.23 \pm 0.03$) and 2 ($\text{WRMSE} = 1.13 \pm 0.02$). The results for *Data noise 3* case are visualized in Fig. 8 and corresponding metrics are shown in Table 4. Comparing the seismic data computed from the posterior I_P and the observed data without noise, the CDPS posterior presents comparatively larger accuracy (WRMSE_d in Table 4 and error distributions in Fig. 8e). However, both predictions have a forward response that is largely within the data error distributions ($\text{WRMSE}_d < 1$). This is also shown by the trace plots in Figure 8f comparing predicted and conditioning data distributions for one vertical trace at $x = 25$ m.

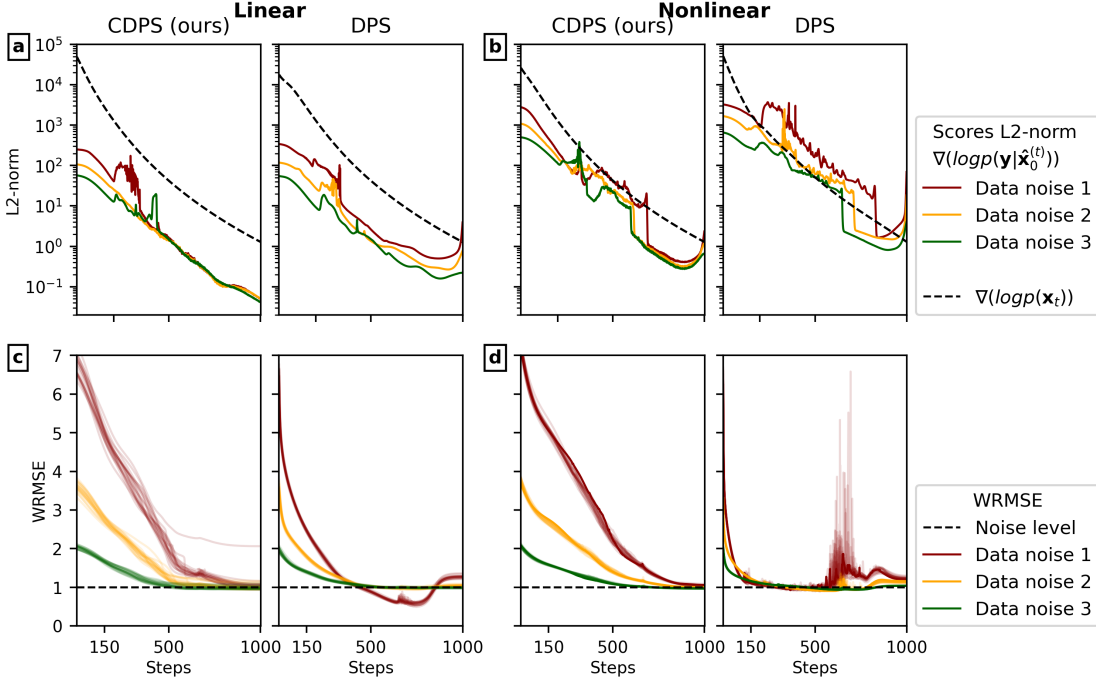


Figure 5: Evolution of prior (dashed) and likelihood (continuous) score functions generative steps, expressed as L2-norm, for (a) linear conditioning and (b) nonlinear conditioning case studies; and WRMSE of 100 samples generated as solutions of the (c) linear and (d) nonlinear inverse problems. The values of magnitude of the three data noise assumed are indicated in Table 2.

Table 4: Metrics of the posterior distributions sampled by CDPS and DPS for the non-linear inversion case, measured for data, facies and I_P (subscripts d , F , and I_P , respectively) for the *Data noise 3* case.

	CDPS	DPS
WRMSE _d	0.34 ± 0.01	0.39 ± 0.01
RMSE _F	0.16	0.19
SSIM _F	0.73 ± 0.03	0.67 ± 0.01
RMSE _{I_P}	3.34×10^5	5.61×10^5
LogS _{I_P}	14.2	36.8
$KL_{I_P}(10^{-3})$	0.5 ± 0.2	1.3 ± 0.2

Overall, the CDPS shows large predictive power; the average facies and I_P generated by CDPS (Fig. 8a and c) retrieve the target with high accuracy (lower RMSE_F and RMSE _{I_P} ; Table 4) and larger variability than DPS (Fig. 8b and d). The generated CDPS facies realizations predict the target facies with accuracies of 98% and 95%, showing a relative improvement compared to the DPS (97% and 94%, respectively), and having a large structural similarity (SSIM_F values in Table 4).

The CDPS has superior prediction accuracy. For the whole study area, the generated ensemble captures the true I_P much better than DPS, as shown by the lower values of logS in Table 4 and in the trace example in Figure 8h ($x = 25$ m). Moreover, each realization reproduces the target I_P -distribution with a low KL divergence (Table 4) and presents fine-scale spatial variability patterns, which appear smoothed in DPS realizations (Fig. 8g).

In an attempt to compare the CDPS results with a high-quality posterior estimate, we ran the pCN method with β -values of 0.1, 0.05, 0.03, and 0.01, using three parallel chains. None of the runs converged to the posterior distribution after 50000 iterations, indicating that the inversion problem is hard, and implicitly suggesting that the CDPS method performs well in practice.

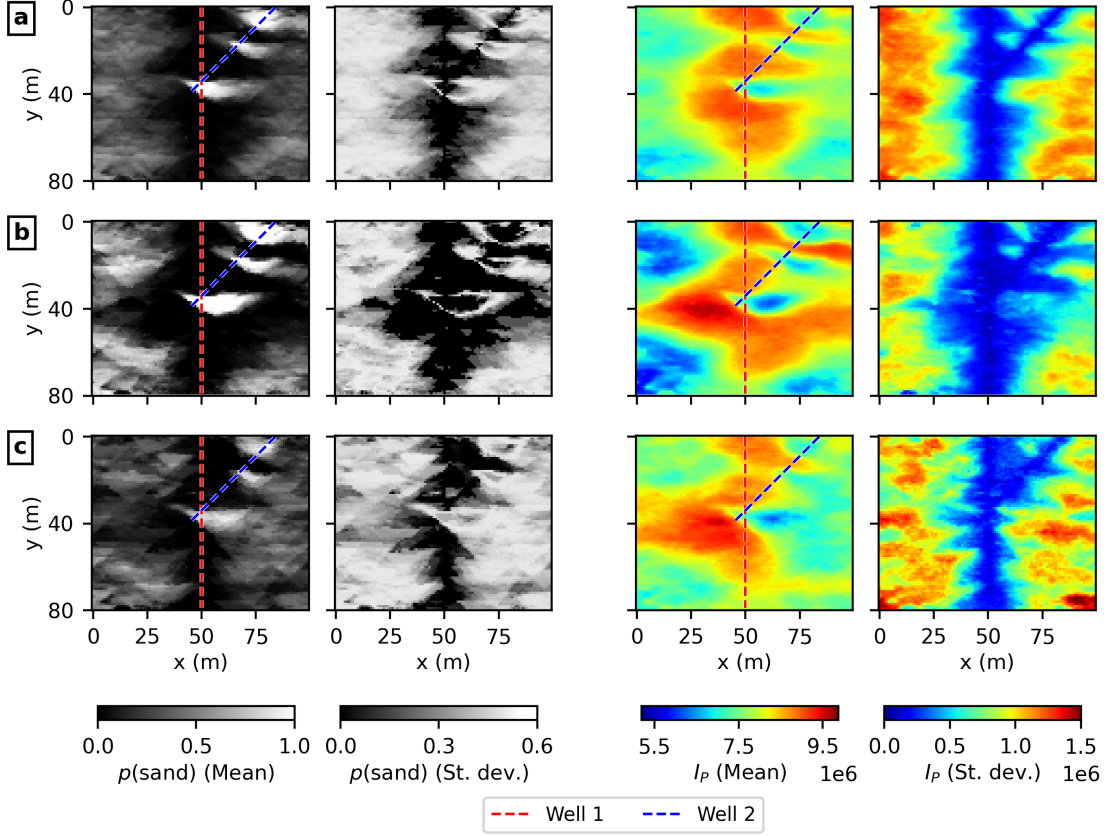


Figure 6: Point-wise average and standard distribution of Facies and I_P posterior samples from (a) CDPS, (b) DPS, (c) pCN MCMC.

3.3 Computational performance

In this study, we did not consider any parallelization (see section 2.5). Moreover, we adopt a 2nd order Heun solver when generating DM samples, and do not evaluate the costs/benefits of using a 1st order solvers (e.g., Euler). The U-Net adopted in the DM (1.31×10^8 trainable parameters) required a total training time of 116 hours (600 epochs); the GAN (1×10^7 parameters) and VAE (3.2×10^7 parameters) took 21 and 10 hours, respectively, to train (2000 epochs). The DM exceeded the modeling accuracy of the fully trained GAN and VAE already at epoch 100, that is, after 19.5 hours of training (see Appendix A).

With EDM, accurate sampling could be obtained when using at least 18 diffusion steps, with no significant improvements observed when considering additional steps. The average generation time of the DM is 3 seconds per multivariate realization (5 to 7 times longer than for GAN and VAE). For the linear conditioning case study (Section 3.2.1), the CDPS and DPS have similar computational time, 0.6 seconds per time step in our tests. The relative time increase, compared to unconditional modeling, is mostly due to the backpropagation computation for the likelihood scores. For the non-linear case (Section 3.2.2), the CDPS had a larger computational cost, requiring 1.5 seconds per denoising step, mostly due to the additional Jacobian matrix computations. After testing different numbers of time-steps (from 18 to 2000 steps), we observed that both CDPS and DPS achieved their best modeling performances using 32 denoising steps. On the other hand, we observed significant differences when considering inversion accuracy for the non-linear case, as summarized in Table 5. Here, the CDPS had a near-optimal performance using 250 steps, while the DPS required a minimum of 1000 steps, which, in our tests, resulted in a significant reduction of the sampling time (approximately half) when considering CDPS, despite its increased computational costs.

The time required by pCN MCMC for the linear case was substantially larger: the burn-in was reached after more than three days of computation, while the poor mixing of the sampled solutions show that much longer sampling would be necessary to recover the full posterior. We do not exclude that other hyperparameter values would improve the performance. The application of pCN on the nonlinear case did not converge in any of the considered cases.

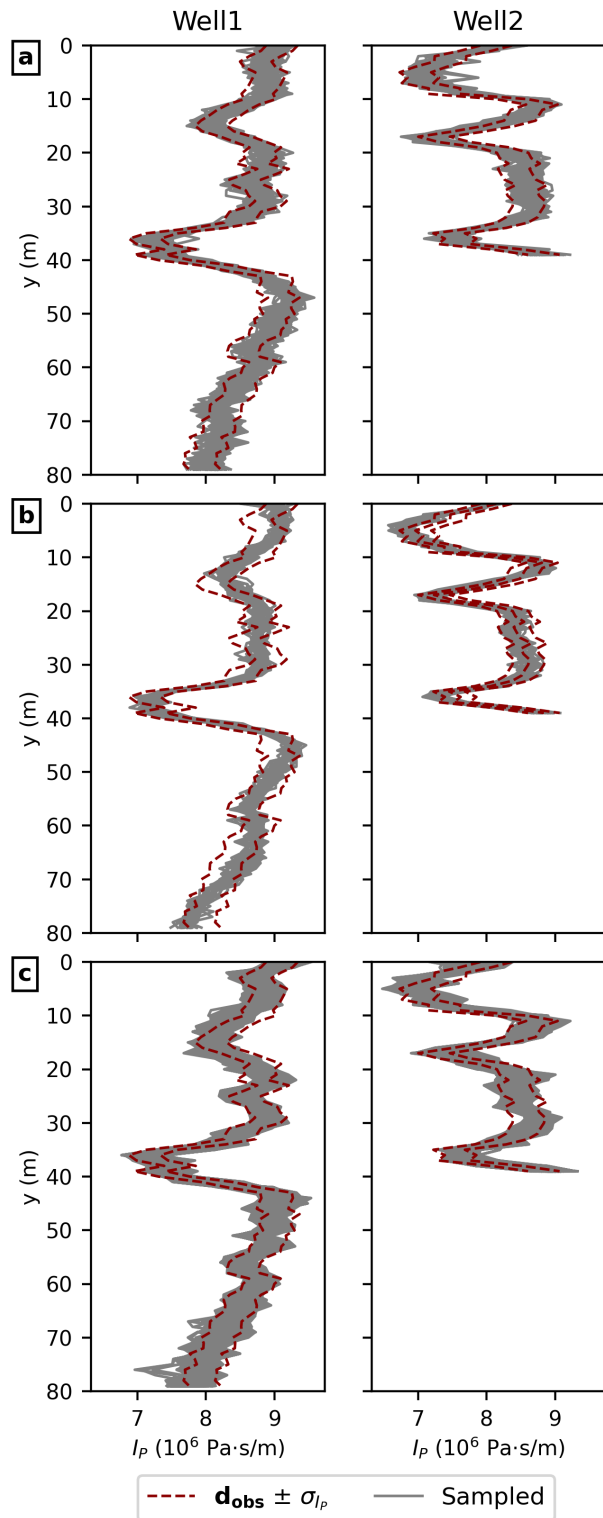


Figure 7: I_P sampled distribution from (a) CDPS, (b) DPS, and (c) pCN MCMC, compared to the expected conditional data distribution $d_{\text{obs}} \pm \sigma_{I_P}$.

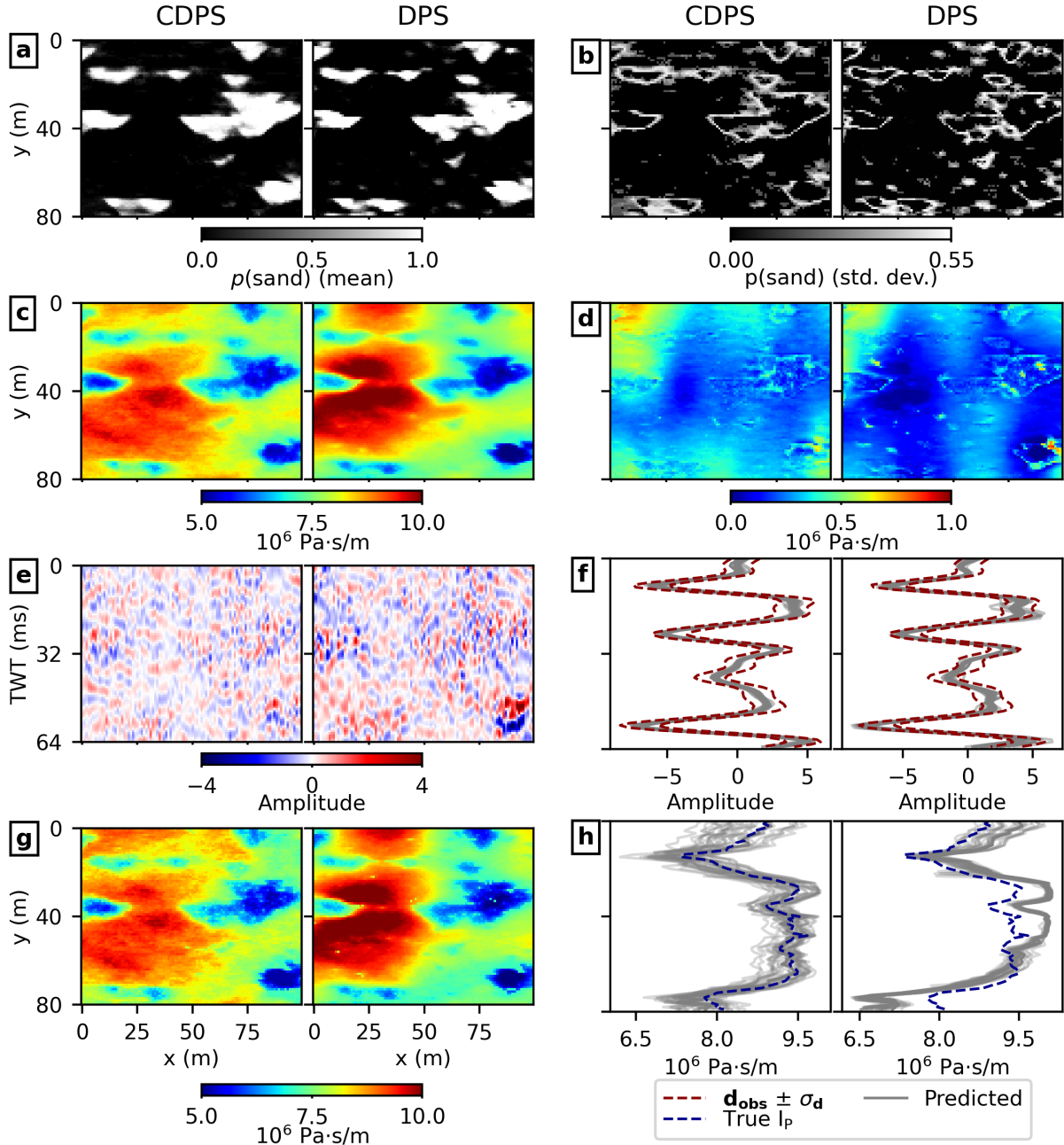


Figure 8: Sampled posterior distribution represented as (a) average facies; (b) facies standard deviation; (c) average I_P ; (d) I_P standard deviation; (e) average data error; (f) predicted data versus conditional data distribution ($d_{\text{obs}} \pm \sigma_d$) for a vertical trace at $x = 25$ m; (g) I_P realizations; (h) I_P samples for a vertical trace at $x = 25$ m compared to the unknown target distribution.

Table 5: WRMSE_d for the three data noise cases considered in the nonlinear inverse modeling (Section 3.2.2); "Div." (Diverged) indicates generative processes diverging to "Not a Number" (NaN) values.

Denoising steps	CDPS			DPS		
	Data noise 1	Data noise 2	Data noise 3	Data noise 1	Data noise 2	Data noise 3
250	1.06±0.03	1.01±0.01	0.998±0.005	Div.	1.30±0.02	1.10±0.02
500	1.05±0.02	0.99±0.01	0.999±0.005	Div.	1.18±0.02	1.17±0.02
1000	1.05±0.02	0.99±0.01	0.997±0.005	1.30±0.03	1.17±0.02	1.054±0.004

4 Discussion

The trained DM effectively samples from complex bivariate geological priors. To evaluate performance, we mainly focused on first- and second-order statistics (higher-order features are considered in the Appendix A). The generated images match the TI features with a fidelity that, to our knowledge, is unprecedented for multivariate geological modeling with deep generative models. For the considered metrics, the DM outperformed the VAE and GAN implementations by Miele et al. [2024] (e.g., Fig. 2 and Table 1), except for a general overestimation of sand volume fraction that was slightly less pronounced in the VAE results (Table 1 and Figure S1 in Appendix A). A practical advantage of DMs for multivariate modeling is the possibility to associate individual channels of the underlying U-Net to specific subsurface property types without the need to modify the network architecture. In contrast, VAE and GAN modeling required independent convolutional layers for each property type. This suggests that pre-designed DM architectures require none or only limited adjustments for modeling different geological scenarios.

The stability of the training process and the high accuracy of DM-based generative modeling come at the cost of high dimensionality and comparatively slow generation times. For instance, the benchmark VAE and GAN perform a compression from 16000 to 60 variables and the corresponding generation times are much faster [Miele et al., 2024]. Modeling biases and errors occur, however, even when considering much lower compression rates, such as in LDMs [Ovanger et al., 2025], highlighting inherent trade-offs between speed, accuracy and dimensionality.

Using the proposed CDPS, pre-trained DMs can be flexibly modified to achieve noise-robust posterior sampling in both linear and non-linear inversion settings. The framework can be used for a wide range of inversion tasks without retraining, and it can deal with the simultaneous use of multiple conditioning data types (Appendix B). The method includes modifications to the DPS by Chung et al. [2023], mainly in terms of an improved likelihood score approximation. By accounting for the error in $\hat{x}_0^{(t)}$ on the simulated conditioning data (Eq. 19), the likelihood scores become more accurate and scaled to diffusion noise (Fig. 5). With this modification, we obtain a much more stable generative process compared to DPS, balancing the two score contributions for posterior sampling (Eq. 10) automatically (i.e., without arbitrary weighting), and making the likelihood score more independent of the data noise. However, a small noise-dependency remains for the nonlinear case with CDPS (Fig. 5b). This might be due to the overly simple assumption of homoscedastic noise in the $\hat{x}_0^{(t)}$ estimates (Fig. 4), which may not hold if the trained network presents any form of localized bias (due to an incorrect training procedure, network's architecture and/or biased TI distributions). Improved error estimates may be needed in future applications, considering locally dependent variances or using approximations of Eq. 15.

Our proposed CDPS algorithm (Algorithm 1) enables efficient and more accurate local conditioning than DPS (see, e.g., Fig. 6a and b). We did not manage to properly benchmark the results against MCMC with pCN proposals (Fig. 6c). Indeed, even in the linear inversion case there is a relatively poor mixing and limited convergence of pCN MCMC; we did not investigate more advanced MCMC approaches such as parallel tempering formulations [Xu et al., 2020]. However, there is an overall good agreement between CDPS and pCN samples at the well locations (Fig. 7 and Table 3). This suggests that CDPS appropriately approximate the posterior. Compared with DPS (Fig. 7b), CDPS (Fig. 7a) has wider uncertainty bounds with magnitudes similar to those obtained by MCMC. We postulate that the underestimation by DPS is primarily a consequence of the likelihood score magnitudes being overestimated (Fig. 5a) when using Eq. 12. For the non-linear inversion case, the CDPS performed well for all considered noise levels while DPS failed when considering low data noise levels (e.g., Fig. 5 and Table 5). Similarly to the linear case, we attribute the unstable DPS denoising trends (Fig. 5) to overestimated likelihood scores, with the overestimation increasing with decreasing data noise.

The DPS used herein is an implementation of the theory by Chung et al. [2023] using the score-based EDM framework. We also considered arbitrarily-weighted Gaussian likelihood functions or the RMSE for the log-score approximation (as in the original DDIM implementation); this led to no convergence and unstable behavior in all the considered cases. We reproduce similar results using CDPS with DDIM (Appendix C) highlighting that the method also works well for this formulation.

Even if the CDPS performs well in practice, it is still an approximate method because the logarithmic score estimate (Eq. 19) relies on an approximation of the intractable likelihood (Eq. 11), the prior score estimates provided by the neural network will inevitably have some errors and the number of diffusion time steps are finite. One computational challenge of the CDPS method is the need to estimate the Jacobian of the forward operator at each time step. When this calculation is expensive, we anticipate that the CDPS approach would still work well in practice even if the Jacobian is only updated occasionally during the generative process.

5 Conclusions

We investigate diffusion models (DM) for sampling multivariate geological priors and propose a modified conditional sampling method (CDPS) for approximate probabilistic Bayesian inversion. The method leverages the iterative nature of diffusion modeling, using an additional likelihood score approximation that modifies the generative process, allowing us to use any pre-trained, unconditional DM. The modeling performances are evaluated on a bivariate distribution of lenticular sand deposits and corresponding acoustic impedances (I_P). The unconditional DM simulations effectively captures first- and second-order statistics, as well as higher-order facies structures represented in training images (TI), consistently outperforming benchmark generative models based on VAEs and GANs. Bayesian posterior sampling is demonstrated for both linear (borehole data) and nonlinear (fullstack seismic) data scenarios, or combinations thereof. Compared to the original Diffusion Posterior Sampling (DPS; Chung et al., 2023), our CDPS implementation provides stabilized inversion across noise levels, as well as more accurate posterior estimates, indicated by lower bias and enhanced exploration of the posterior pdf. The method also shows significant advantages over an MCMC formulation in terms of convergence, leading to vastly decreased computing times. This work highlights the strengths of diffusion-based generative models for complex subsurface modeling and inference tasks. The training is much more robust than for GANs and the data generation quality is beyond the capabilities of GANs and VAEs. The CDPS approach enables flexible and scalable probabilistic inversion with minimal architectural tuning, resulting in an approximate Bayesian inversion method with broad applications across complex geological scenarios and data types.

6 Code availability

The implementation of CDPS for EDM is available at https://github.com/romiele/CDPS_EDM. The corresponding CDPS inversion using DDPM and DDIM frameworks are available at https://github.com/romiele/CDPS_DDIM.

References

Dario Grana, Tapan Mukerji, and Philippe Doyen. *Seismic Reservoir Modeling: Theory, Examples, and Algorithms*. Wiley, 1 edition, April 2021. ISBN 978-1-119-08618-5 978-1-119-08621-5. doi: 10.1002/9781119086215.

Yoram Rubin and Susan Sharpless Hubbard. *Hydrogeophysics*. Number v. 50 in Water Science and Technology Library. Springer, Dordrecht [Netherlands] New York, 2005. ISBN 978-1-4020-3102-1.

Albert Tarantola. *Inverse Problem Theory and Methods for Model Parameter Estimation*. Society for Industrial and Applied Mathematics, January 2005. ISBN 978-0-89871-572-9 978-0-89871-792-1. doi: 10.1137/1.9780898717921.

Niklas Linde, David Ginsbourger, James Irving, Fabio Nobile, and Arnaud Doucet. On uncertainty quantification in hydrogeology and hydrogeophysics. *Advances in Water Resources*, 110:166–181, December 2017. ISSN 03091708. doi: 10.1016/j.advwatres.2017.10.014.

J.Jaime Gómez-Hernández and Xian-Huan Wen. To be or not to be multi-Gaussian? A reflection on stochastic hydrogeology. *Advances in Water Resources*, 21(1):47–61, February 1998. ISSN 03091708. doi: 10.1016/S0309-1708(96)00031-0.

Insa Neuweiler, Alexandros Papafotiou, Holger Class, and Rainer Helmig. Estimation of effective parameters for a two-phase flow problem in non-Gaussian heterogeneous porous media. *Journal of Contaminant Hydrology*, 120–121:141–156, March 2011. ISSN 01697722. doi: 10.1016/j.jconhyd.2010.08.001.

Andre G. Journel and Clayton V. Deutsch. Entropy and spatial disorder. *Mathematical Geology*, 25(3):329–355, April 1993. ISSN 0882-8121, 1573-8868. doi: 10.1007/BF00901422.

Fengde Zhou, Daren Shields, Stephen Tyson, and Joan Esterle. Comparison of sequential indicator simulation, object modelling and multiple-point statistics in reproducing channel geometries and continuity in 2D with two different spaced conditional datasets. *Journal of Petroleum Science and Engineering*, 166:718–730, July 2018. ISSN 09204105. doi: 10.1016/j.petrol.2018.03.043.

Felipe B. Guardiano and R. Mohan Srivastava. Multivariate Geostatistics: Beyond Bivariate Moments. In F. M. Gradstein and Amilcar Soares, editors, *Geostatistics Tróia '92*, volume 5, pages 133–144. Springer Netherlands, Dordrecht, 1993. ISBN 978-0-7923-2157-6 978-94-011-1739-5. doi: 10.1007/978-94-011-1739-5_12.

Sebastien Strebelle. Conditional Simulation of Complex Geological Structures Using Multiple-Point Statistics. *Mathematical Geology*, 34(1):1–21, January 2002. ISSN 1573-8868. doi: 10.1023/A:1014009426274.

Gregoire Mariethoz, Philippe Renard, and Julien Straubhaar. The Direct Sampling method to perform multiple-point geostatistical simulations. *Water Resources Research*, 46(11):2008WR007621, November 2010a. ISSN 0043-1397, 1944-7973. doi: 10.1029/2008WR007621.

Gregoire Mariethoz and Jef Caers. *Multiple-Point Geostatistics: Stochastic Modeling with Training Images*. Wiley, 1 edition, October 2014. ISBN 978-1-118-66275-5 978-1-118-66295-3. doi: 10.1002/9781118662953.

Anne-Sophie Høyer, Giulio Vignoli, Thomas Mejer Hansen, Le Thanh Vu, Donald A. Keefer, and Flemming Jørgensen. Multiple-point statistical simulation for hydrogeological models: 3-D training image development and conditioning strategies. *Hydrology and Earth System Sciences*, 21(12):6069–6089, December 2017. ISSN 1607-7938. doi: 10.5194/hess-21-6069-2017.

Mathieu Le Coz, Jacques Bodin, and Philippe Renard. On the use of multiple-point statistics to improve groundwater flow modeling in karst aquifers: A case study from the Hydrogeological Experimental Site of Poitiers, France. *Journal of Hydrology*, 545:109–119, February 2017. ISSN 00221694. doi: 10.1016/j.jhydrol.2016.12.010.

Julien Straubhaar, Philippe Renard, and Tatiana Chugunova. Multiple-point statistics using multi-resolution images. *Stochastic Environmental Research and Risk Assessment*, 34(2):251–273, February 2020. ISSN 1436-3240, 1436-3259. doi: 10.1007/s00477-020-01770-8.

Yulia Melnikova, Andrea Zunino, Katrine Lange, Knud Skou Cordua, and Klaus Mosegaard. History Matching Through a Smooth Formulation of Multiple-Point Statistics. *Mathematical Geosciences*, 47(4):397–416, May 2015. ISSN 1874-8961, 1874-8953. doi: 10.1007/s11004-014-9537-y.

Jef Caers and Tuanfeng Zhang. Multiple-point Geostatistics: A Quantitative Vehicle for Integrating Geologic Analogs into Multiple Reservoir Models. In G. Michael Grammer, Paul M. “Mitch” Harris, and Gregor P. Eberli, editors, *Integration of Outcrop and Modern Analogs in Reservoir Modeling*, pages 383–394. American Association of Petroleum Geologists, 2004. ISBN 978-0-89181-361-3 978-1-62981-047-8. doi: 10.1306/M80924C18.

Julien Straubhaar, Philippe Renard, and Grégoire Mariethoz. Conditioning multiple-point statistics simulations to block data. *Spatial Statistics*, 16:53–71, May 2016. ISSN 22116753. doi: 10.1016/j.spasta.2016.02.005.

Thomas Mejer Hansen, Le Thanh Vu, Klaus Mosegaard, and Knud Skou Cordua. Multiple point statistical simulation using uncertain (soft) conditional data. *Computers & Geosciences*, 114:1–10, May 2018. ISSN 00983004. doi: 10.1016/j.cageo.2018.01.017.

Julien Straubhaar and Philippe Renard. Conditioning Multiple-Point Statistics Simulation to Inequality Data. *Earth and Space Science*, 8(5):e2020EA001515, May 2021. ISSN 2333-5084, 2333-5084. doi: 10.1029/2020EA001515.

Tobias Zahner, Tobias Lochbühler, Grégoire Mariethoz, and Niklas Linde. Image synthesis with graph cuts: A fast model proposal mechanism in probabilistic inversion. *Geophysical Journal International*, 204(2):1179–1190, February 2016. ISSN 0956-540X, 1365-246X. doi: 10.1093/gji/ggv517.

Shiran Levy, Lea Friedli, Grégoire Mariéthoz, and Niklas Linde. Conditioning of multiple-point statistics simulations to indirect geophysical data. *Computers & Geosciences*, 187:105581, May 2024. ISSN 00983004. doi: 10.1016/j.cageo.2024.105581.

Eric Laloy, Niklas Linde, Diederik Jacques, and Grégoire Mariethoz. Merging parallel tempering with sequential geostatistical resampling for improved posterior exploration of high-dimensional subsurface categorical fields. *Advances in Water Resources*, 90:57–69, April 2016. ISSN 03091708. doi: 10.1016/j.advwatres.2016.02.008.

Thomas Mejer Hansen, Knud Skou Cordua, and Klaus Mosegaard. Inverse problems with non-trivial priors: Efficient solution through sequential Gibbs sampling. *Computational Geosciences*, 16(3):593–611, June 2012. ISSN 1420-0597, 1573-1499. doi: 10.1007/s10596-011-9271-1.

Grégoire Mariethoz, Philippe Renard, and Jef Caers. Bayesian inverse problem and optimization with iterative spatial resampling. *Water Resources Research*, 46(11):2010WR009274, November 2010b. ISSN 0043-1397, 1944-7973. doi: 10.1029/2010WR009274.

Ian Goodfellow, Yoshua Bengio, and Aaron Courville. *Deep Learning*. Adaptive Computation and Machine Learning. The MIT press, Cambridge, Mass, 2016. ISBN 978-0-262-03561-3.

Diederik P. Kingma and Max Welling. Auto-Encoding Variational Bayes. In *International Conference on Learning Representations*, December 2013.

Ian J. Goodfellow, Jean Pouget-Abadie, Mehdi Mirza, Bing Xu, David Warde-Farley, Sherjil Ozair, Aaron Courville, and Yoshua Bengio. Generative Adversarial Networks, June 2014.

Eric Laloy, Romain Héault, John Lee, Diederik Jacques, and Niklas Linde. Inversion using a new low-dimensional representation of complex binary geological media based on a deep neural network. *Advances in Water Resources*, 110:387–405, December 2017. ISSN 03091708. doi: 10.1016/j.advwatres.2017.09.029.

Eric Laloy, Romain Héault, Diederik Jacques, and Niklas Linde. Training-Image Based Geostatistical Inversion Using a Spatial Generative Adversarial Neural Network. *Water Resources Research*, 54(1):381–406, January 2018. ISSN 0043-1397, 1944-7973. doi: 10.1002/2017WR022148.

Alain Oliviero-Durmus, Yazid Janati, and Marcelo Pereyra. Generative modelling meets Bayesian inference: A new paradigm for inverse problems. *Philosophical transactions of the Royal Society A*, 383(2299), June 2025.

Shiran Levy, Jürg Hunziker, Eric Laloy, James Irving, and Niklas Linde. Using deep generative neural networks to account for model errors in Markov chain Monte Carlo inversion. *Geophysical Journal International*, 228(2): 1098–1118, October 2021. ISSN 0956-540X, 1365-246X. doi: 10.1093/gji/ggab391.

Lukas Mosser, Olivier Dubrule, and Martin J. Blunt. Stochastic Seismic Waveform Inversion Using Generative Adversarial Networks as a Geological Prior. *Mathematical Geosciences*, 52(1):53–79, January 2020. ISSN 1874-8961, 1874-8953. doi: 10.1007/s11004-019-09832-6.

Mingliang Liu, Dario Grana, and Leandro Passos De Figueiredo. Uncertainty quantification in stochastic inversion with dimensionality reduction using variational autoencoder. *GEOPHYSICS*, 87(2):M43–M58, March 2022. ISSN 0016-8033, 1942-2156. doi: 10.1190/geo2021-0138.1.

Arnaud Doucet, Nando Freitas, and Neil Gordon, editors. *Sequential Monte Carlo Methods in Practice*. Springer New York, New York, NY, 2001. ISBN 978-1-4419-2887-0 978-1-4757-3437-9. doi: 10.1007/978-1-4757-3437-9.

M Amaya, N Linde, and E Laloy. Adaptive sequential Monte Carlo for posterior inference and model selection among complex geological priors. *Geophysical Journal International*, 226(2):1220–1238, May 2021. ISSN 0956-540X, 1365-246X. doi: 10.1093/gji/ggab170.

Smith W.A. Canchumuni, Alexandre A. Emerick, and Marco Aurélio C. Pacheco. Towards a robust parameterization for conditioning facies models using deep variational autoencoders and ensemble smoother. *Computers & Geosciences*, 128:87–102, July 2019. ISSN 00983004. doi: 10.1016/j.cageo.2019.04.006.

Mingliang Liu and Dario Grana. Petrophysical characterization of deep saline aquifers for CO₂ storage using ensemble smoother and deep convolutional autoencoder. *Advances in Water Resources*, 142:103634, August 2020. ISSN 03091708. doi: 10.1016/j.advwatres.2020.103634.

Shaoxing Mo, Nicholas Zabaras, Xiaoqing Shi, and Jichun Wu. Integration of Adversarial Autoencoders With Residual Dense Convolutional Networks for Estimation of Non-Gaussian Hydraulic Conductivities. *Water Resources Research*, 56(2):e2019WR026082, February 2020. ISSN 0043-1397, 1944-7973. doi: 10.1029/2019WR026082.

Eric Laloy, Niklas Linde, Cyprien Ruffino, Romain Héault, Gilles Gasso, and Diederik Jacques. Gradient-based deterministic inversion of geophysical data with generative adversarial networks: Is it feasible? *Computers & Geosciences*, 133:104333, December 2019. ISSN 00983004. doi: 10.1016/j.cageo.2019.104333.

Emilien Dupont, Tuanfeng Zhang, Peter Tilke, Lin Liang, and William Bailey. Generating Realistic Geology Conditioned on Physical Measurements with Generative Adversarial Networks, July 2018.

Shing Chan and Ahmed H. Elsheikh. Parametric generation of conditional geological realizations using generative neural networks. *Computational Geosciences*, 23(5):925–952, October 2019. ISSN 1420-0597, 1573-1499. doi: 10.1007/s10596-019-09850-7.

Shiran Levy, Eric Laloy, and Niklas Linde. Variational Bayesian inference with complex geostatistical priors using inverse autoregressive flows. *Computers & Geosciences*, 171:105263, February 2023. ISSN 00983004. doi: 10.1016/j.cageo.2022.105263.

Roberto Miele, Shiran Levy, Niklas Linde, Amilcar Soares, and Leonardo Azevedo. Deep generative networks for multivariate fullstack seismic data inversion using inverse autoregressive flows. *Computers & Geosciences*, 188: 105622, June 2024. ISSN 00983004. doi: 10.1016/j.cageo.2024.105622.

L. Mosser, O. Dubrule, and M.J. Blunt. Conditioning of Generative Adversarial Networks for Pore and Reservoir Scale Models. In *Proceedings*, Copenhagen, Denmark, June 2018. EAGE Publications BV. doi: 10.3997/2214-4609.201800774.

Chengkai Zhang, Xianzhi Song, and Leonardo Azevedo. U-net generative adversarial network for subsurface facies modeling. *Computational Geosciences*, 25(1):553–573, February 2021. ISSN 1420-0597, 1573-1499. doi: 10.1007/s10596-020-10027-w.

Eric Laloy, Niklas Linde, and Diederik Jacques. Approaching geoscientific inverse problems with vector-to-image domain transfer networks, November 2020.

Runhai Feng, Klaus Mosegaard, Dario Grana, Tapan Mukerji, and Thomas Mejer Hansen. Stochastic Facies Inversion with Prior Sampling by Conditional Generative Adversarial Networks Based on Training Image. *Mathematical Geosciences*, 56(4):665–690, May 2024. ISSN 1874-8961, 1874-8953. doi: 10.1007/s11004-023-10119-0.

Roberto Miele and Leonardo Azevedo. Physics-informed W-Net GAN for the direct stochastic inversion of fullstack seismic data into facies models. *Scientific Reports*, 14(1):5122, March 2024. ISSN 2045-2322. doi: 10.1038/s41598-024-55683-5.

Mario Lucic, Karol Kurach, Marcin Michalski, Olivier Bousquet, and Sylvain Gelly. Are GANs created equal? a large-scale study. In *Proceedings of the 32nd International Conference on Neural Information Processing Systems*, NIPS’18, pages 698–707, Red Hook, NY, USA, December 2018. Curran Associates Inc.

Jorge Lopez-Alvis, Eric Laloy, Frédéric Nguyen, and Thomas Hermans. Deep generative models in inversion: A review and development of a new approach based on a variational autoencoder. *Computers & Geosciences*, 152: 104762, July 2021. ISSN 00983004. doi: 10.1016/j.cageo.2021.104762.

Jonathan Ho, Ajay Jain, and Pieter Abbeel. Denoising diffusion probabilistic models. In *Proceedings of the 34th International Conference on Neural Information Processing Systems*, NIPS ’20, pages 6840–6851, Red Hook, NY, USA, December 2020. Curran Associates Inc. ISBN 978-1-7138-2954-6.

Jascha Sohl-Dickstein, Eric A. Weiss, Niru Maheswaranathan, and Surya Ganguli. Deep Unsupervised Learning using Nonequilibrium Thermodynamics. In *Proceedings of the 32nd International Conference on Machine Learning*, November 2015.

Prafulla Dhariwal and Alex Nichol. Diffusion Models Beat GANs on Image Synthesis, June 2021.

Jiaming Song, Chenlin Meng, and Stefano Ermon. Denoising Diffusion Implicit Models. In *Proceedings of the International Conference on Learning Representations*, 2021a.

Yang Song, Jascha Sohl-Dickstein, Diederik P. Kingma, Abhishek Kumar, Stefano Ermon, and Ben Poole. Score-Based Generative Modeling through Stochastic Differential Equations. In *Thirty-Seventh Conference on Neural Information Processing Systems*, 2021b. doi: 10.48550/arXiv.2011.13456.

Tero Karras, Miika Aittala, Timo Aila, and Samuli Laine. Elucidating the Design Space of Diffusion-Based Generative Models. In *36th Conference on Neural Information Processing Systems*, October 2022.

L. Mosser. Deep Diffusion Models for Facies Modeling. In *84th EAGE Annual Conference & Exhibition Workshop Programme*, pages 1–5, Vienna, Austria, 2023. European Association of Geoscientists & Engineers. doi: 10.3997/2214-4609.2023101627.

Emiel Hoogeboom, Alexey A. Gritsenko, Jasmijn Bastings, Ben Poole, Rianne van den Berg, and Tim Salimans. Autoregressive Diffusion Models. In *International Conference on Learning Representations*, February 2022. doi: 10.48550/arXiv.2110.02037.

Minghui Xu, Suihong Song, and Tapan Mukerji. DiffSim: Denoising diffusion probabilistic models for generative facies geomodeling. In *Fourth International Meeting for Applied Geoscience & Energy*, pages 1660–1664, Houston, Texas, July 2024. Society of Exploration Geophysicists and American Association of Petroleum Geologists. doi: 10.1190/image2024-4081304.1.

Ali Aouf, Eric Laloy, Bart Rogiers, and Christophe De Vleeschouwer. 3D clay microstructure synthesis using Denoising Diffusion Probabilistic Models. *Applied Computing and Geosciences*, 26:100248, June 2025. ISSN 25901974. doi: 10.1016/j.acags.2025.100248.

Daesoo Lee, Oscar Ovanger, Jo Eidsvik, Erlend Aune, Jacob Skauvold, and Ragnar Hauge. Latent Diffusion Model for Conditional Reservoir Facies Generation. *Computers & Geosciences*, 194:105750, January 2025. ISSN 00983004. doi: 10.1016/j.cageo.2024.105750.

Robin Rombach, Andreas Blattmann, Dominik Lorenz, Patrick Esser, and Bjorn Ommer. High-Resolution Image Synthesis with Latent Diffusion Models. In *2022 IEEE/CVF Conference on Computer Vision and Pattern Recognition (CVPR)*, pages 10674–10685, New Orleans, LA, USA, June 2022. IEEE. doi: 10.1109/cvpr52688.2022.01042.

Oscar Ovanger, Daesoo Lee, Jo Eidsvik, Ragnar Hauge, Jacob Skauvold, and Erlend Aune. A Statistical Study of Latent Diffusion Models for Geological Facies Modeling. *Mathematical Geosciences*, February 2025. ISSN 1874-8961, 1874-8953. doi: 10.1007/s11004-025-10178-5.

G. Matheron, H. Beucher, C. De Fouquet, A. Galli, D. Guerillot, and C. Ravenne. Conditional Simulation of the Geometry of Fluvio-Deltaic Reservoirs. In *SPE Annual Technical Conference and Exhibition*, pages SPE-16753-MS, Dallas, Texas, September 1987. SPE. doi: 10.2118/16753-MS.

Trond Mannseth. Relation Between Level Set and Truncated Pluri-Gaussian Methodologies for Facies Representation. *Mathematical Geosciences*, 46(6):711–731, August 2014. ISSN 1874-8961, 1874-8953. doi: 10.1007/s11004-013-9507-9.

Fu Wang, Xinquan Huang, and Tariq A. Alkhalifah. A Prior Regularized Full Waveform Inversion Using Generative Diffusion Models. *IEEE Transactions on Geoscience and Remote Sensing*, 61:1–11, 2023. ISSN 0196-2892, 1558-0644. doi: 10.1109/TGRS.2023.3337014.

Mohammad H. Taufik, Fu Wang, and Tariq Alkhalifah. Learned Regularizations for Multi-Parameter Elastic Full Waveform Inversion Using Diffusion Models. *Journal of Geophysical Research: Machine Learning and Computation*, 1(1):e2024JH000125, March 2024. ISSN 2993-5210, 2993-5210. doi: 10.1029/2024JH000125.

Fu Wang, Xinquan Huang, and Tariq Alkhalifah. Controllable Seismic Velocity Synthesis Using Generative Diffusion Models. *Journal of Geophysical Research: Machine Learning and Computation*, 1(3):e2024JH000153, September 2024. ISSN 2993-5210, 2993-5210. doi: 10.1029/2024JH000153.

Guido Di Federico and Louis J. Durlofsky. Latent diffusion models for parameterization of facies-based geomodels and their use in data assimilation. *Computers & Geosciences*, 194:105755, January 2025. ISSN 00983004. doi: 10.1016/j.cageo.2024.105755.

Giannis Daras, Hyungjin Chung, Chieh-Hsin Lai, Yuki Mitsufuji, Jong Chul Ye, Peyman Milanfar, Alexandros G. Dimakis, and Mauricio Delbracio. A Survey on Diffusion Models for Inverse Problems, September 2024.

Zheng Zhao, Ziwei Luo, Jens Sjölund, and Thomas Schön. Conditional sampling within generative diffusion models. *Philosophical transactions of the Royal Society A*, 383(2299), June 2025. doi: 10.1098/rsta.2024.0329.

Jonathan Ho and Tim Salimans. Classifier-Free Diffusion Guidance. In *NeurIPS 2021 Workshop on Deep Generative Models and Downstream Applications*, December 2021.

Jay Whang, Mauricio Delbracio, Hossein Talebi, Chitwan Saharia, Alexandros G. Dimakis, and Peyman Milanfar. Deblurring via Stochastic Refinement. In *2022 IEEE/CVF Conference on Computer Vision and Pattern Recognition (CVPR)*, pages 16272–16282, New Orleans, LA, USA, June 2022. IEEE. ISBN 978-1-6654-6946-3. doi: 10.1109/CVPR52688.2022.01581.

Guan-Horng Liu, Arash Vahdat, De-An Huang, Evangelos A. Theodorou, Weili Nie, and Anima Anandkumar. $\mathbb{I}^2\mathbb{S}\mathbb{B}$: Image-to-Image Schrödinger Bridge. In *Proceedings of the 40th International Conference on Machine Learning*, May 2023. doi: 10.48550/arXiv.2302.05872.

Morteza Mardani, Jiaming Song, Jan Kautz, and Arash Vahdat. A Variational Perspective on Solving Inverse Problems with Diffusion Models. In *The Twelfth International Conference on Learning Representations*, October 2023.

Cagan Alkan, Julio Oscanoa, Daniel Abraham, Mengze Gao, Aizada Nurdinova, Kawin Setsompop, John M. Pauly, Morteza Mardani, and Shreyas Vasanawala. Variational Diffusion Models for Blind MRI Inverse Problems. In *NeurIPS 2023 Workshop on Deep Learning and Inverse Problems*, November 2023.

Berthy Feng and Katherine Bouman. Variational Bayesian Imaging with an Efficient Surrogate Score-based Prior. In *Transactions on Machine Learning Research*, March 2024.

Brian L. Trippe, Jason Yim, Doug Tischer, David Baker, Tamara Broderick, Regina Barzilay, and Tommi S. Jaakkola. Diffusion Probabilistic Modeling of Protein Backbones in 3D for the motif-scaffolding problem. In *The Eleventh International Conference on Learning Representations*, September 2022.

Gabriel Cardoso, Yazid Janati el Idrissi, Sylvain Le Corff, and Eric Moulines. Monte Carlo guided Denoising Diffusion models for Bayesian linear inverse problems. In *The Twelfth International Conference on Learning Representations*, October 2023.

Luhuan Wu, Brian L. Trippe, Christian A. Naesseth, David M. Blei, and John P. Cunningham. Practical and Asymptotically Exact Conditional Sampling in Diffusion Models. In *Neural Information Processing Systems*, 2024.

Zehao Dou and Yang Song. Diffusion posterior sampling for linear inverse problem solving — a filtering perspective. In *The Twelfth International Conference on Learning Representations*, 2024.

Hyungjin Chung, Jeongsol Kim, Michael Thompson Mccann, Marc Louis Klasky, and Jong Chul Ye. Diffusion posterior sampling for general noisy inverse problems. In *The 11th International Conference on Learning Representations*, 2023.

Shayan Mohajer Hamidi and En-Hui Yang. Enhancing Diffusion Models for Inverse Problems with Covariance-Aware Posterior Sampling. In *The 13th International Conference on Learning Representations*, 2025.

Benjamin Boys, Mark Girolami, Jakiw Pidstrigach, Sebastian Reich, Alan Mosca, and O. Deniz Akyildiz. Tweedie Moment Projected Diffusions For Inverse Problems. *Transactions on Machine Learning Research*, September 2024.

Nebiyou Yismaw, Ulugbek S Kamilov, and M Salman Asif. Gaussian is all you need: A unified framework for solving inverse problems via diffusion posterior sampling. *IEEE Transactions on Computational Imaging*, 2025.

Jiaming Song, Arash Vahdat, Morteza Mardani, and Jan Kautz. Pseudoinverse-guided diffusion models for inverse problems. In *International Conference on Learning Representations*, 2023.

S. L. Cotter, G. O. Roberts, A. M. Stuart, and D. White. MCMC Methods for Functions: Modifying Old Algorithms to Make Them Faster. *Statistical Science*, 28(3), August 2013. ISSN 0883-4237. doi: 10.1214/13-STS421.

Yang Song and Stefano Ermon. Generative modeling by estimating gradients of the data distribution. In H. Wallach, H. Larochelle, A. Beygelzimer, F. dAlché-Buc, E. Fox, and R. Garnett, editors, *Advances in Neural Information Processing Systems*, volume 32. Curran Associates, Inc., 2019.

Brian D.O. Anderson. Reverse-time diffusion equation models. *Stochastic Processes and their Applications*, 12(3): 313–326, May 1982. ISSN 03044149. doi: 10.1016/0304-4149(82)90051-5.

Herbert Robbins. An empirical Bayes approach to statistics. In *Berkeley Symposium on Mathematical Statistics and Probability*, pages 157–163. University of California Press, 1956.

Bradley Efron. Tweedie’s Formula and Selection Bias. *Journal of the American Statistical Association*, 106(496): 1602–1614, December 2011. ISSN 0162-1459, 1537-274X. doi: 10.1198/jasa.2011.tm11181.

Tongda Xu, Xiyan Cai, Xinjie Zhang, Xingtong Ge, Dailan He, Ming Sun, Jingjing Liu, Ya-Qin Zhang, Jian Li, and Yan Wang. Rethinking Diffusion Posterior Sampling: From Conditional Score Estimator to Maximizing a Posterior. In *The Thirteenth International Conference on Learning Representations*, 2025.

Xinyu Peng, Ziyang Zheng, Wenrui Dai, Nuoqian Xiao, Chenglin Li, Junni Zou, and Hongkai Xiong. Improving Diffusion Models for Inverse Problems Using Optimal Posterior Covariance. In *The 12th International Conference on Learning Representations*, June 2024.

Lea Friedli and Niklas Linde. Solving Geophysical Inversion Problems with Intractable Likelihoods: Linearized Gaussian Approximations Versus the Correlated Pseudo-marginal Method. *Mathematical Geosciences*, 56(1):55–75, January 2024. ISSN 1874-8961, 1874-8953. doi: 10.1007/s11004-023-10064-y.

Uri M. Ascher and Linda R. Petzold. *Computer Methods for Ordinary Differential Equations and Differential-Algebraic Equations*. Society for Industrial and Applied Mathematics, Philadelphia, PA, January 1998. ISBN 978-0-89871-412-8 978-1-61197-139-2. doi: 10.1137/1.9781611971392.

Olaf Ronneberger, Philipp Fischer, and Thomas Brox. U-Net: Convolutional Networks for Biomedical Image Segmentation, May 2015.

Ashish Vaswani, Noam Shazeer, Niki Parmar, Jakob Uszkoreit, Llion Jones, Aidan N Gomez, Łukasz Kaiser, and Illia Polosukhin. Attention is All you Need. *31st Conference on Neural Information Processing Systems (NIPS 2017)*, 2017.

S. Kullback and R. A. Leibler. On Information and Sufficiency. *The Annals of Mathematical Statistics*, 22(1):79–86, March 1951. ISSN 0003-4851. doi: 10.1214/aoms/1177729694.

Zhou Wang, A.C. Bovik, H.R. Sheikh, and E.P. Simoncelli. Image quality assessment: From error visibility to structural similarity. *IEEE Transactions on Image Processing*, 13(4):600–612, April 2004. ISSN 1057-7149, 1941-0042. doi: 10.1109/TIP.2003.819861.

I. J. Good. Rational Decisions. *Journal of the Royal Statistical Society Series B: Statistical Methodology*, 14(1): 107–114, January 1952. ISSN 1369-7412, 1467-9868. doi: 10.1111/j.2517-6161.1952.tb00104.x.

Andrew Gelman and Donald B. Rubin. Inference from Iterative Simulation Using Multiple Sequences. *Statistical Science*, 7(4):457–472, 1992. ISSN 0883-4237.

Rúben Nunes, Amílcar Soares, Leonardo Azevedo, and Pedro Pereira. Geostatistical Seismic Inversion with Direct Sequential Simulation and Co-simulation with Multi-local Distribution Functions. *Mathematical Geosciences*, 49 (5):583–601, July 2017. ISSN 1874-8961, 1874-8953. doi: 10.1007/s11004-016-9651-0.

Amílcar Soares. Direct Sequential Simulation and Cosimulation. *Mathematical Geology*, 33(8):911–926, November 2001. ISSN 0882-8121, 1573-8868. doi: 10.1023/a:1012246006212.

Teng Xu, Sebastian Reuschen, Wolfgang Nowak, and Harrie-Jan Hendricks Franssen. Preconditioned Crank-Nicolson Markov Chain Monte Carlo Coupled With Parallel Tempering: An Efficient Method for Bayesian Inversion of Multi-Gaussian Log-Hydraulic Conductivity Fields. *Water Resources Research*, 56(8), August 2020. ISSN 0043-1397, 1944-7973. doi: 10.1029/2020wr027110.

Clayton V Deutsch and Andre G Journel. Geostatistical software library and user’s guide. *New York*, 119(147):578, 1992.

Appendix

A Additional assessment of prior modeling performance

A.1 Geostatistical metrics

We further assessed the performance of unconditional modeling of the DM based on geological and geostatistical criteria. To evaluate the ability of the generative method to reproduce the channels' morphologies, Table 6 summarizes the average and standard deviations of length, thickness and area of the sandy channels, as they are represented in the prior TI and reproduced by the DM, GAN and VAE. Here, the DM shows superior modeling ability, especially compared to the VAE where the unconditional modeling is expected to output unrealistic realizations [see, e.g., Levy et al., 2023, Miele et al., 2024, Lopez-Alvis et al., 2021]. We also observed that the realizations generated by the DM slightly overestimate the proportion of sands (0.29 ± 0.04) compared to the targeted prior (0.27 ± 0.05); VAE and GAN perform better (0.28 ± 0.03 and 0.28 ± 0.04 , respectively) (Fig. 9a).

Table 6: Measures for facies morphology computed from 500 prior/unconditional facies realizations.

	Length (m)	Thickness (m)	Area (m^2)
Prior	17.5 ± 4.3	5.9 ± 1.3	113 ± 33
DM	17.4 ± 4.4	5.9 ± 1.4	118 ± 36
GAN	16.2 ± 3.6	5.6 ± 1.2	105 ± 30
VAE	8.9 ± 1.6	3.3 ± 0.6	53 ± 13

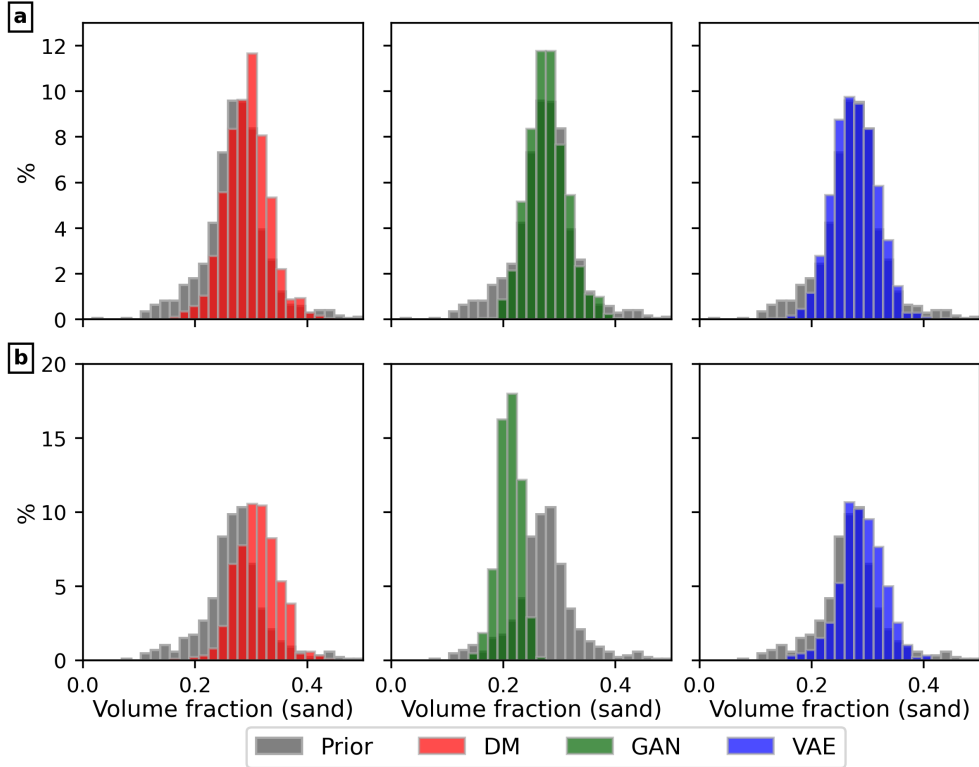


Figure 9: Volume fraction of sands in the generated realizations, compared to TI (Prior), for (a) the fully trained models, and (b) for early training stages at epoch 100.

We further computed the spatial uncertainty patterns of the generated I_P distributions as experimental variograms along the horizontal and vertical directions, from 60 realizations. The I_P distributions in the TI were generated considering facies-dependent spatial patterns. For sands we used an exponential model, with maximum distance of significant spatial correlation [ranges; e.g., Deutsch and Journel, 1992] of 50 m and 25 m along horizontal and

vertical directions, respectively. For shales, we use a spherical variogram model with ranges of 65 m (horizontal direction) and 25 m (vertical direction). Due to the channels heterogeneity, the facies-dependent I_P spatial patterns are affected by truncations at large ranges and their corresponding experimental variograms show disagreements with the theoretical models. However, we qualitatively estimate if spatial patterns are reproduced, by obtaining the experimental variograms from 100 TI samples and I_P realizations generated with DM, GAN and VAE. The results are shown in Figure 10, where the experimental points are linearly interpolated for visual aid. Overall, we see a good match between the DM and the prior, with noticeable improvements for the I_P distribution in the shale.

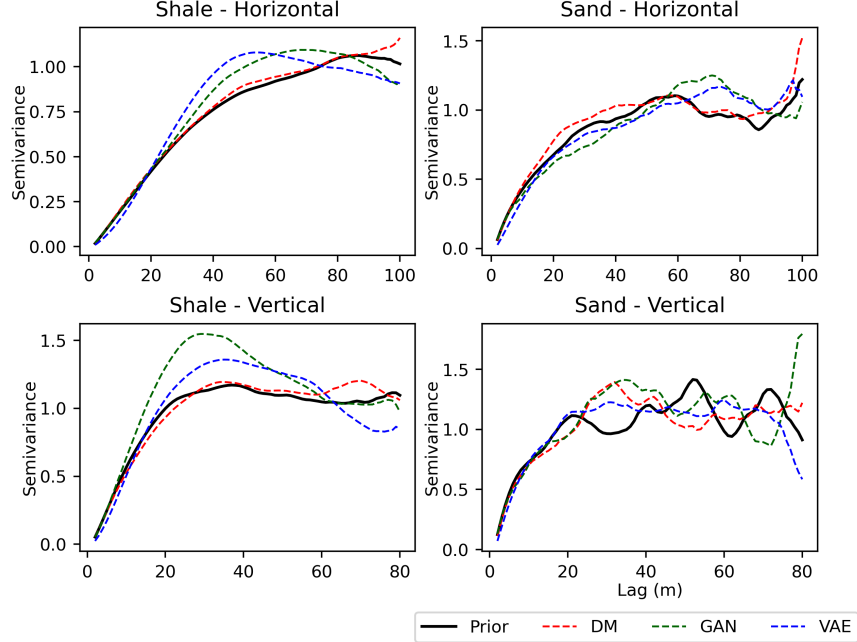


Figure 10: Experimental variograms, per facies and direction, computed from 60 I_P prior and models realizations.

A.2 Training efficiency

Diffusion models generally have a larger computational costs than GANs and VAEs. This is reflected, for example in the total training time of the proposed DM (4 days and 15h for 600 epochs) compared to the other generative models (respectively, 21h for the GAN and 12h for the VAE for 2000 epochs each). While we adopted a long training time for the three model to maximize their accuracy (Fig. 11), we observe that the training of the DM is significantly more efficient. Already at epoch 100 (i.e., after 19h of training), the DM approximates the prior first- and second- order statistics with sufficient accuracy (Table 7, Fig. 12 and Fig. 9b) and it is generally more accurate than the fully trained GAN which required a similar training time.

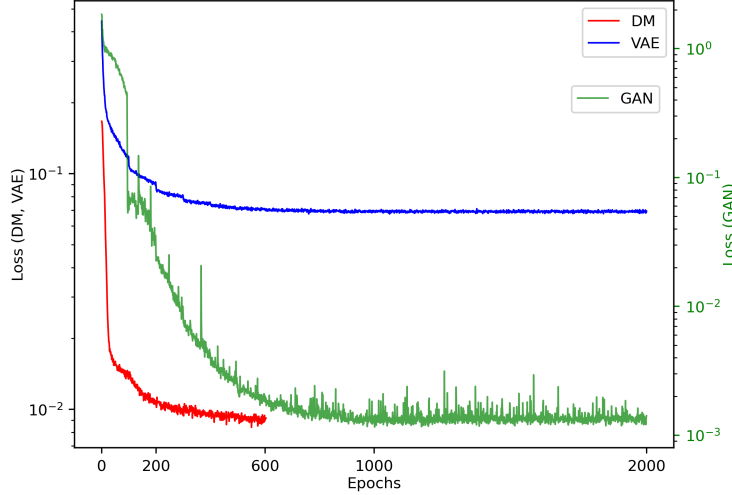


Figure 11: Loss values for the three trained networks. DM and VAE have comparable loss metrics (data mean squared error), GAN has an adversarial loss.

Table 7: Metrics for unconditional prior modeling using the trained DM and benchmarking GAN and VAE at epoch 100. $p(\text{sand})$ and Avg. I_P refer to the average models obtained from the realizations ensembles. KL : Kullback–Leibler divergence; Avg.: average; St. dev.: standard deviation.

		$p(\text{sand})$ — Avg. I_P	I_P marginal distributions	
		Relative error	Avg. \pm St. dev. ($10^6 \text{ Pa} \cdot \text{s/m}$)	KL_{I_P}
Prior	<i>Sand</i>	-	6.66 ± 0.73	-
	<i>Shale</i>		8.54 ± 0.66	-
DM	<i>Sand</i>	15.0%	0.665 ± 0.73	$0.8\text{e-}3$
	<i>Shale</i>	0.82%	0.853 ± 0.67	$0.9\text{e-}3$
GAN	<i>Sand</i>	58.0%	0.662 ± 0.65	$2.3\text{e-}3$
	<i>Shale</i>	3.8%	0.853 ± 0.63	$1.4\text{e-}3$
VAE	<i>Sand</i>	12.3%	0.686 ± 0.70	$1.4\text{e-}3$
	<i>Shale</i>	1.2%	0.862 ± 0.68	$1.8\text{e-}3$

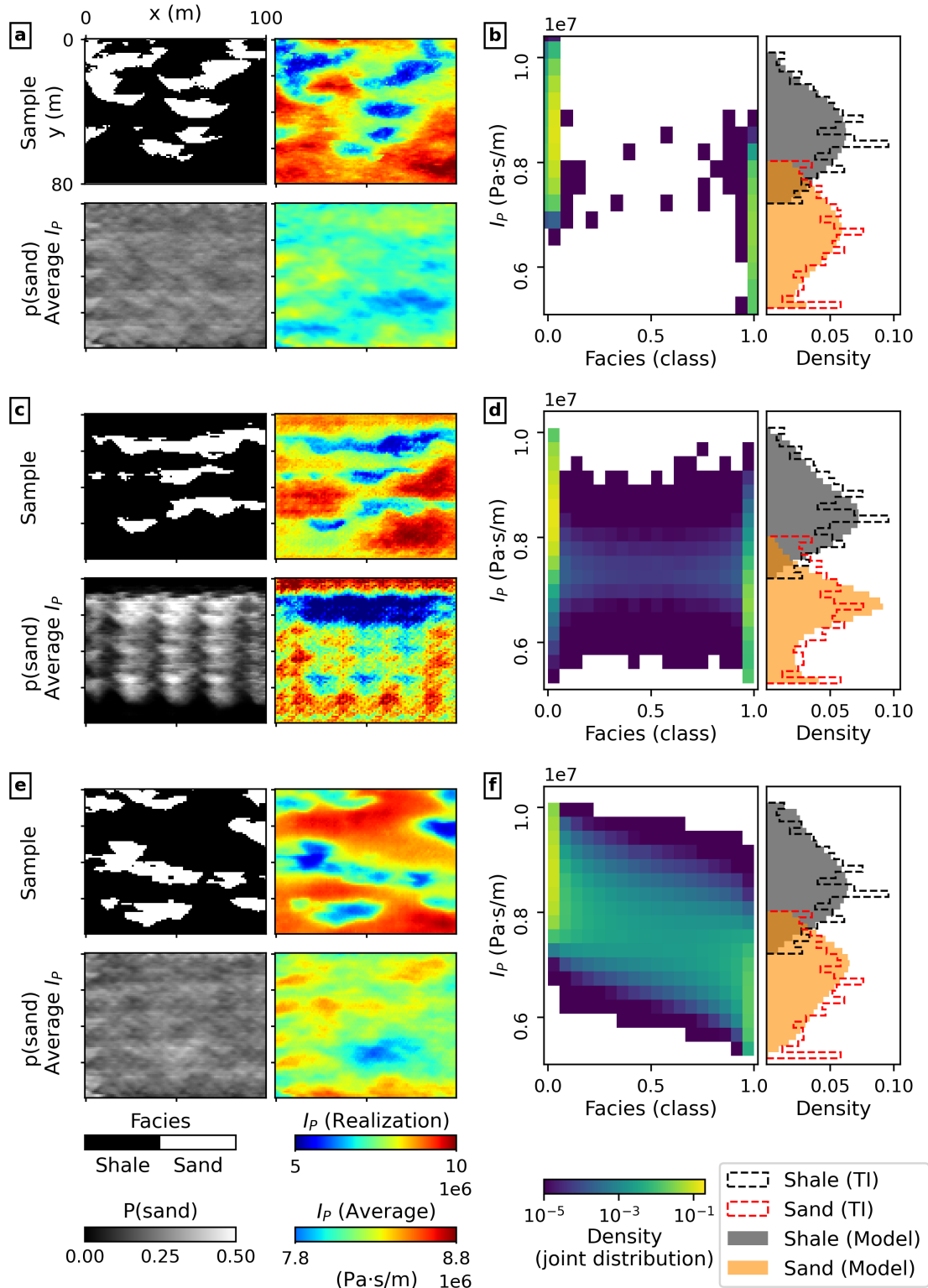


Figure 12: Summary of unconditional modeling performances of (a, b) DM, (c, d) GAN, and (e, f) VAE at training epoch 100. Subplots (a), (c), (e): realizations and average distribution of facies and I_P for (a) DM, (c) GAN and (e) VAE; subplots (b), (d), (f): joint and I_P distributions for (b) DM, (d) GAN and (f) VAE.

B Conditioning on multiple data types

We applied the CDPS algorithm on three different test cases (*Target* in Fig. 13a, b, c) using both direct observations (well logs) and seismic reflection data; the location of the well is shown in Fig. 13 as red dashed line. The conditioning data has Gaussian uncorrelated noise with amplitude corresponding to the *Data noise 2* (Table 2 in Section 3.2). Conditioning on two data types required computing the corresponding likelihood scores, individually, and summing them to the prior score for the denoising at each time-step. For these applications we considered 300 steps. The target used as *Case 1* (Fig. 13a) represents a scenario not included in our TI, having only a single channel body in the facies distribution (2% in sand volume fraction). This can be seen as an example of inversion when the prior knowledge is biased; *Case 2* and *Case 3* (Fig. 13b and c, respectively) are test example extracted from the TI (not used during training).

Figures 13 and 14 summarize the solutions obtained, showing the results from 50 generated samples; the accuracy of the inversion solutions is described in Table 8 using the same metrics shown in Section 3.2.2. In all the cases, we observe a good convergence of the solutions, with all the samples having WRMSE (when compared to the noiseless data) < 1 (WRMSE_d in Table 8). The solutions retrieved honor the conditioning data within the uncertainty ranges, in both well data and seismic data domains (Fig. 14): at the well location ($x = 50$ m in Fig. 14), the I_P values fit the uncertainty range, while the corresponding seismic data shows lower variability than the considered error standard deviation, especially at larger seismic amplitudes. A similar pattern is observed at locations where only seismic data conditioning is used (e.g., $x = 25$ m in Fig. 14). Given the close match between the predicted and noiseless seismic data, this behavior suggests that the relative component of the seismic uncertainty does not significantly impact the inversion results.

Both facies and I_P distributions match the target with good accuracy in the studied area (Fig. 14). Overall, the facies realizations generated match the target with an accuracy of 94% for *Case 1* and 96% for *Case 2* and *Case 3*, with a large structural similarity to the target (SSIM_F in Table 8). The $p(\text{sand})$ and average I_P computed from the realizations ensembles (Fig. 13) match the targets, and their corresponding standard deviation shows larger variability mostly at facies interfaces. The standard deviation of I_P realizations (*Std. dev.* in Fig. 13) also highlights the lateral conditioning of the well log data. For *Case 1*, few solutions predict the presence of sands in the upper left area (an area of lower I_P values), significantly mismatching the target; here, we also see larger variability of the solutions (Fig. 13 and, e.g., I_P trace at $x = 25$ m in Fig. 14a). This can be interpreted as an effect of the bias of the trained DM compared to this case study.

Overall, the predictive power of the CDPS is large, with good results for the biased *Case 1*, as shown by the comparably close values of all the metrics in Table 8. The *Case 2* shows relatively poorer performances of the CDPS in I_P distribution prediction. The realizations present lower variability (Figures 13b and 14b), and their ensemble not always match well to the local true I_P , hence the higher logS measured values (Table 8).

Table 8: Metrics of the posterior distributions sampled by CDPS, measured for data, facies and I_P (subscripts d, F, and I_P , respectively), for the three studied cases assuming *Data noise 2*.

	Case 1	Case 2	Case 3
WRMSE _d	0.204±0.005	0.199±0.006	0.201±0.06
RMSE _F	0.19	0.20	0.21
SSIM _F	0.73±0.05	0.72±0.02	0.69±0.02
RMSE _{I_P}	4.50×10^5	3.58×10^5	3.24×10^5
LogS _{I_P}	14.5	18.7	14.2
$KL_{I_P} (10^{-4})$	6.3±1.5	3.5±0.5	3.8±0.8

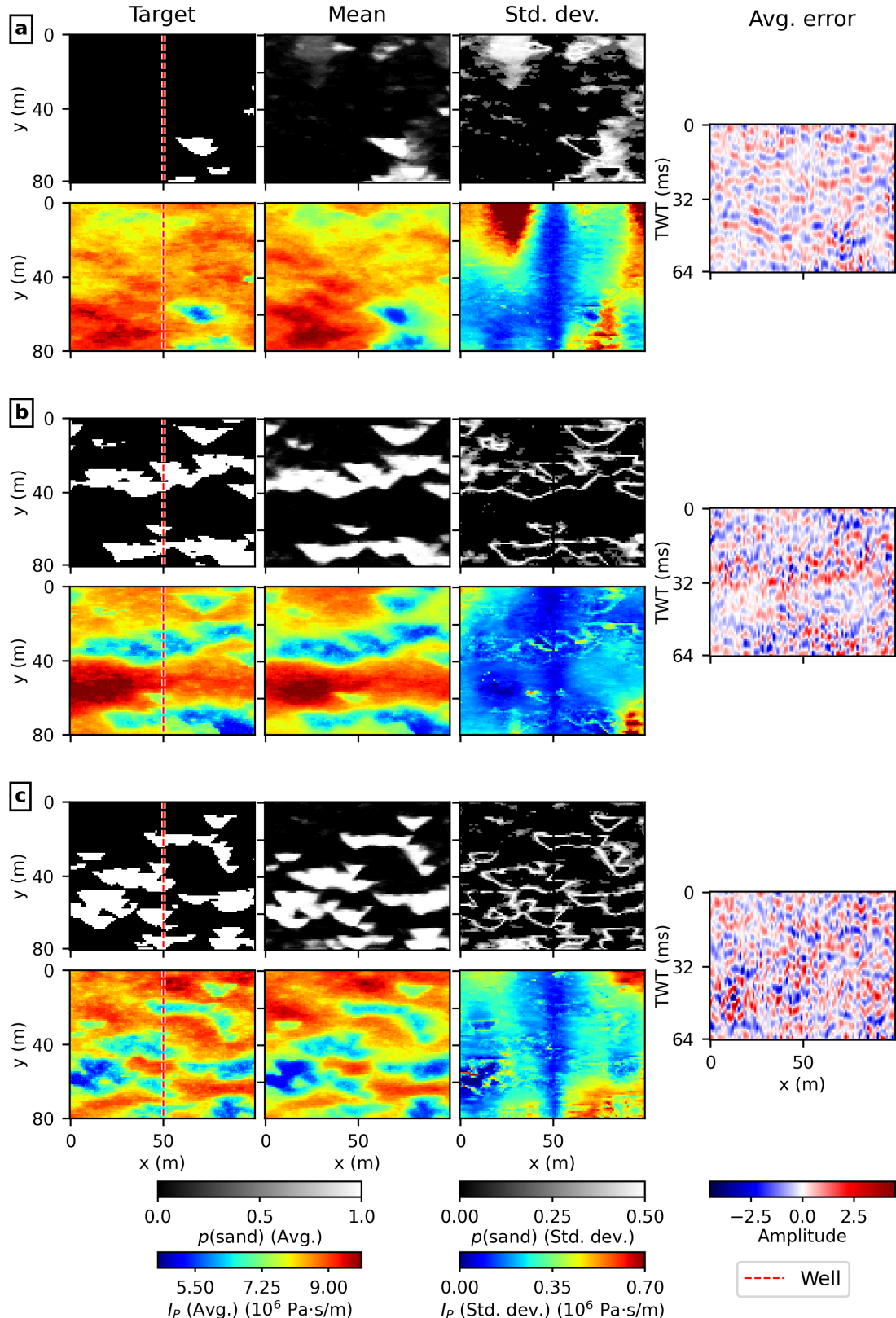


Figure 13: Target and posterior facies and I_P for the three inversion case studies (a, b, c) using both well logs and seismic data as conditioning data. The sampled posterior distribution is shown as mean and standard deviation (*Std. dev.*) of realizations' ensembles, and corresponding average seismic data misfit.

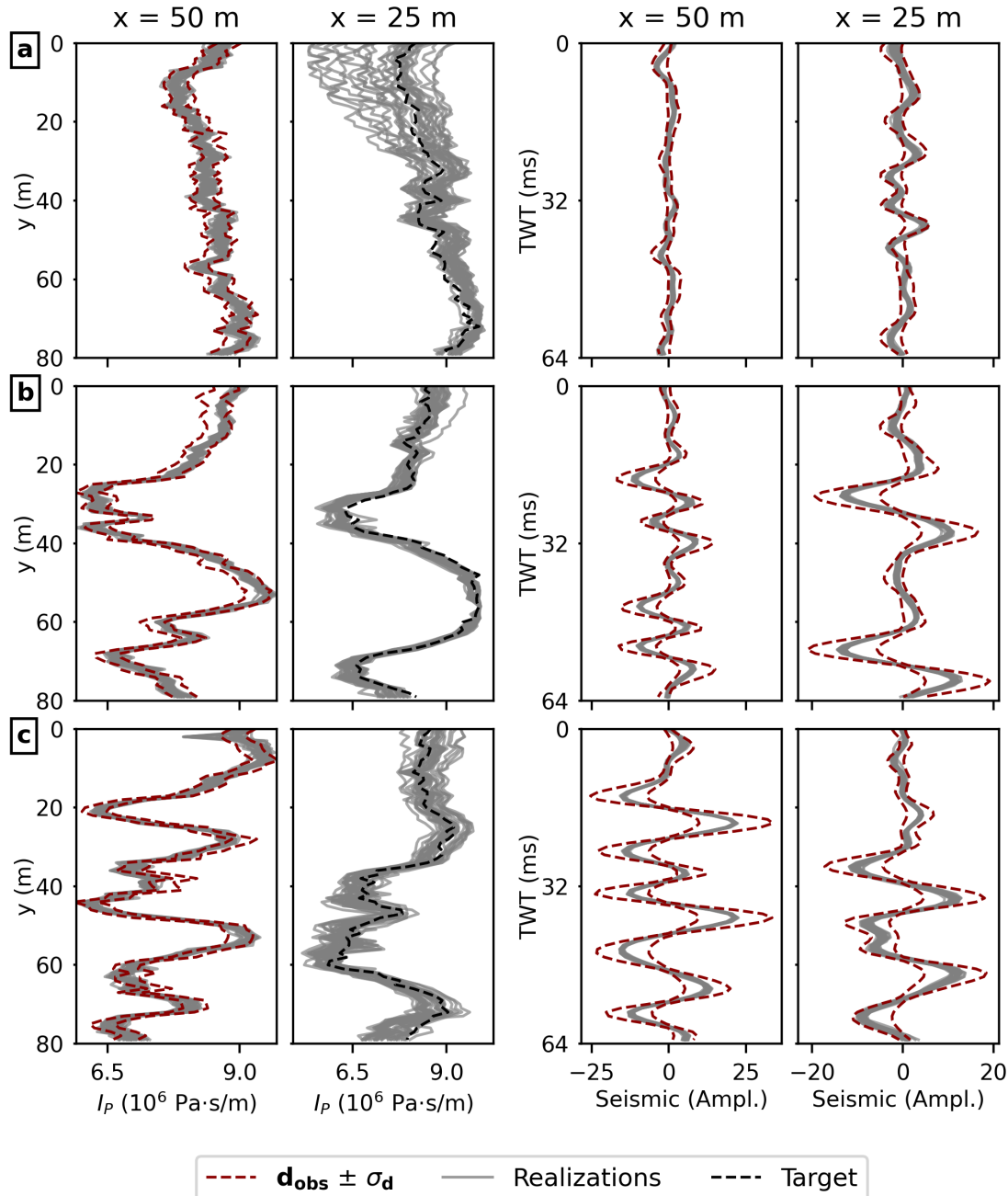


Figure 14: Predicted I_P and corresponding seismic data along vertical traces located at the well location ($x = 50 \text{ m}$) and at $x = 25 \text{ m}$, for the three inversion case studies (a, b, c). The predictions are compared with conditioning data d_{obs} and unknown true I_P (Target).

C CDPS implementation with DDPM and DDIM

We implement the CDPS in the DDPM and DDIM frameworks, shown in Algorithm 2. Differently from score-based diffusion, the trained network predicts the noise added to a sample, denoted as ϵ_θ . This can be related to the score function using the following correlation [Dhariwal and Nichol, 2021]

$$\nabla_{x_t} \log p_t(\mathbf{x}_t) = -\frac{1}{\sqrt{1-\bar{\alpha}_t}} \epsilon_\theta^{(t)}, \quad (25)$$

where $\bar{\alpha}_t$ is inversely correlated to the diffusion noise (See Section 2.1 and Ho et al. [2020]). Therefore, to integrate the likelihood score within the DDPM and DDIM frameworks, we rescale it to $\sqrt{(1-\bar{\alpha}_t)} \nabla_{x_t} \log p_t(\mathbf{d}|\mathbf{x}_t)$ (line 19 of Algorithm 2). We then sum the two components as

$$\hat{\epsilon}^{(t)} = \epsilon_\theta^{(t)} - \sqrt{(1-\bar{\alpha}_t)} \nabla_{x_t} \log p_t(\mathbf{d}|\mathbf{x}_t), \quad (26)$$

and use this "posterior-related" drift to obtain the denoised \mathbf{x}_{t-1} . This approach was first proposed by Dhariwal and Nichol [2021] in their guided diffusion modeling. For the application of the CDPS with DDIM, we use the same diffusion UNet described in Section 2.3 and retrain it using the same TI for noise prediction; the training parameters and process are the same described in Dhariwal and Nichol [2021].

Using one well as conditioning data, contaminated with Gaussian noise of magnitude equal to the case *Data noise 2* (Table 2 in Section 3.2), we sampled 100 samples using CDPS (Algorithm 2) and the DPS method in its original implementation, with weight $\rho = 1$ as defined for the inpainting tasks. Using CDPS with either DDIM (deterministic) or DDPM (stochastic) sampling did not change the results; we used the DPS in its original implementation with DDPM. For both CDPS and DPS, we sampled with 1000 denoising steps. The results are summarized in Fig. 15. All the realizations using CDPS match the conditioning facies with 100% of accuracy and have WRMSE = 0.7 ± 0.2 ; in the unconditioned area between $x = 0$ m and $x = 20$ m, the $p(\text{sand}) = 0.28$. These values are closer to the prior than our linear conditioning case with score-based diffusion (Section 3.2.1); we attribute this difference to the absence of the second conditioning well. For DPS, we observe that the data is perfectly matching the noisy data (overfitting), with standard deviation approaching 0. This does not occur in our implementation of the DPS with score-based diffusion, as the likelihood score magnitude is rescaled proportionally to the diffusion noise content, hence is less *influential* on the conditioning diffusion. The lack of such rescaling is, in fact, the inconsistency between conditional diffusion theory and the original DPS implementation on DDPM we highlight in Section 2.2.1. Our CDPS (Algorithm 2) integrates this correction.

We further applied the methods for fullstack seismic data inverse modeling. We show here the results for a nonlinear inverse problem equal to that use in Section 3.2.2, considering the *data noise 2*. For DPS, we show the results considering a likelihood score weight $\rho = 0.4$, corresponding to that suggested by Chung et al. [2023] for nonlinear phase retrieval. For both CDPS and DPS, we sampled with 1000 denoising steps. The results are summarized in Fig. 16 and integrated with the metrics of Table 9. The DPS showed high instability of the denoising process; the CDPS underperformed compared to the equivalent score-based inverse problem. Although we did not investigate the possible causes for such difference, we believe that assumptions of an isotropic uncertainty for the denoiser may play a role in the inversion accuracy for the nonlinear case.

Table 9: Metrics of the posterior distributions sampled by CDPS and DPS, measured for data, facies and I_P (subscripts \mathbf{d} , \mathbf{F} , and I_P , respectively).

	CDPS	DPS
WRMSE _d	0.70 ± 0.01	7.1 ± 0.6
RMSE _F	0.19	0.24
SSIM _F	0.60 ± 0.04	0.51 ± 0.15
RMSE _{I_P}	4.47×10^5	4.19×10^5
LogS _{I_P}	14.0	16.0
$KL_{I_P} (10^{-3})$	0.4 ± 0.1	3.1 ± 1.1

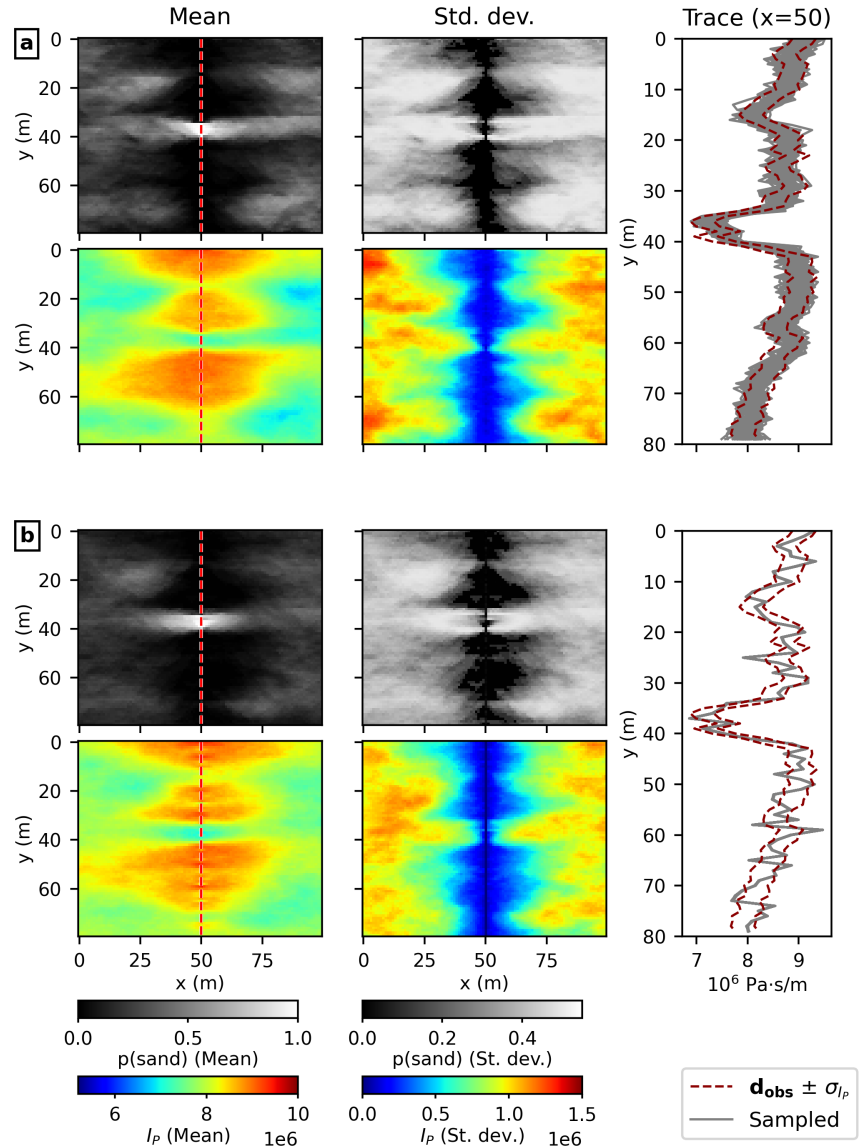


Figure 15: Conditioned realizations sampled using (a) CDPS and (b) DPS, represented as mean and standard deviation (Std. dev.) of facies and I_P distributions, and sampled I_P at the conditioning well location ($x=50$ m).

Algorithm 2 Corrected DPS algorithm for DDPM (Gaussian error)

1: **Require:** trained network $S_\theta(\mathbf{x}_t, t)$, conditioning data \mathbf{d} , forward operator \mathcal{F} , noise schedule $\{\sigma\}_{t=1}^N$ and $\{\beta\}_{t=1}^N$
(with $\alpha = 1 - \beta$)

2: **for** $t = T, \dots, 1$ **do**
 3: **sample** $\mathbf{x}_0 \sim q_{data}$
 4: $\mathbf{x}_t \leftarrow \alpha_t \mathbf{x}_0 + (1 - \alpha_t) \mathbf{z}$, $\mathbf{z} \sim \mathcal{N}(0, I)$
 5: $\epsilon_\theta^{(t)} \leftarrow S_\theta(\mathbf{x}_t, t)$
 6: $\hat{\mathbf{x}}_0^{(t)} \leftarrow \left(\mathbf{x}_t - \sqrt{1 - \bar{\alpha}_t} \epsilon_\theta^{(t)} \right) / \sqrt{\bar{\alpha}_t}$
 7: $\sigma_{\hat{\mathbf{x}}_0}^{(t)} \leftarrow \mathbb{E} \left[\sqrt{\sum_{i=1}^N (\hat{x}_{0,i}^{(t)} - x_{0,i})^2 / N} \right]$
 8: **end for**

9: **sample** $\mathbf{x}_T \sim \mathcal{N}(0, I)$
 10: **for** $t = T-1, \dots, 0$ **do**
 11: $\epsilon_\theta^{(t)} \leftarrow S_\theta(\mathbf{x}_t, t)$
 12: $\hat{\mathbf{x}}_0^{(t)} \leftarrow \left(\mathbf{x}_t - \sqrt{1 - \bar{\alpha}_t} \epsilon_\theta^{(t)} \right) / \sqrt{\bar{\alpha}_t}$
 13: **if** \mathcal{F} is nonlinear **then**
 14: $\mathcal{J}_{\hat{\mathbf{x}}_0} \leftarrow \mathcal{J}_{\mathcal{F}}(\hat{\mathbf{x}}_0^{(t)})$
 15: $\tilde{\Sigma}_{\mathbf{d}} \leftarrow \mathcal{J}_{\hat{\mathbf{x}}_0^{(t)}}^T \Sigma_{\hat{\mathbf{x}}_0^{(t)}} \mathcal{J}_{\hat{\mathbf{x}}_0^{(t)}} + \Sigma_{\mathbf{d}}$
 16: **else**
 17: $\tilde{\Sigma}_{\mathbf{d}} \leftarrow \mathcal{F}^T \Sigma_{\hat{\mathbf{x}}_0^{(t)}} \mathcal{F} + \Sigma_{\mathbf{d}}$
 18: **end if**
 19: $\nabla_{x_t} \log p_t(\mathbf{d} | \hat{\mathbf{x}}_0^{(t)}) \leftarrow -\nabla_{\mathbf{x}_t} \left[(\mathcal{F}(\hat{\mathbf{x}}_0^{(t)}) - \mathbf{d})^T \tilde{\Sigma}_{\mathbf{d}}^{-1} (\mathcal{F}(\hat{\mathbf{x}}_0^{(t)}) - \mathbf{d}) \right]$
 20: $\hat{\epsilon}^{(t)} \leftarrow \epsilon_\theta^{(t)} + \sqrt{(1 - \bar{\alpha}_t)} \nabla_{x_t} \log p_t(\mathbf{x}_t)$
 21: $\mathbf{z} \sim \mathcal{N}(0, I)$
 22: $x_{t-1} \leftarrow \frac{\sqrt{\alpha_t}(1 - \bar{\alpha}_{t-1})}{1 - \bar{\alpha}_{t-1}} \mathbf{x}_t + \frac{\sqrt{\alpha_{t-1}} \beta_t}{1 - \bar{\alpha}_{t-1}} \left(\mathbf{x}_t - \sqrt{1 - \bar{\alpha}_t} \nabla_{x_t} \log p_t(\hat{\mathbf{x}}_0^{(t)} | \mathbf{d}) \right) / \sqrt{\bar{\alpha}_t} + \sigma_t \mathbf{z}$
 23: **end for**
 24: **Output:** $\tilde{\mathbf{x}}_0 \sim p(\mathbf{x}_0 | \mathbf{d})$

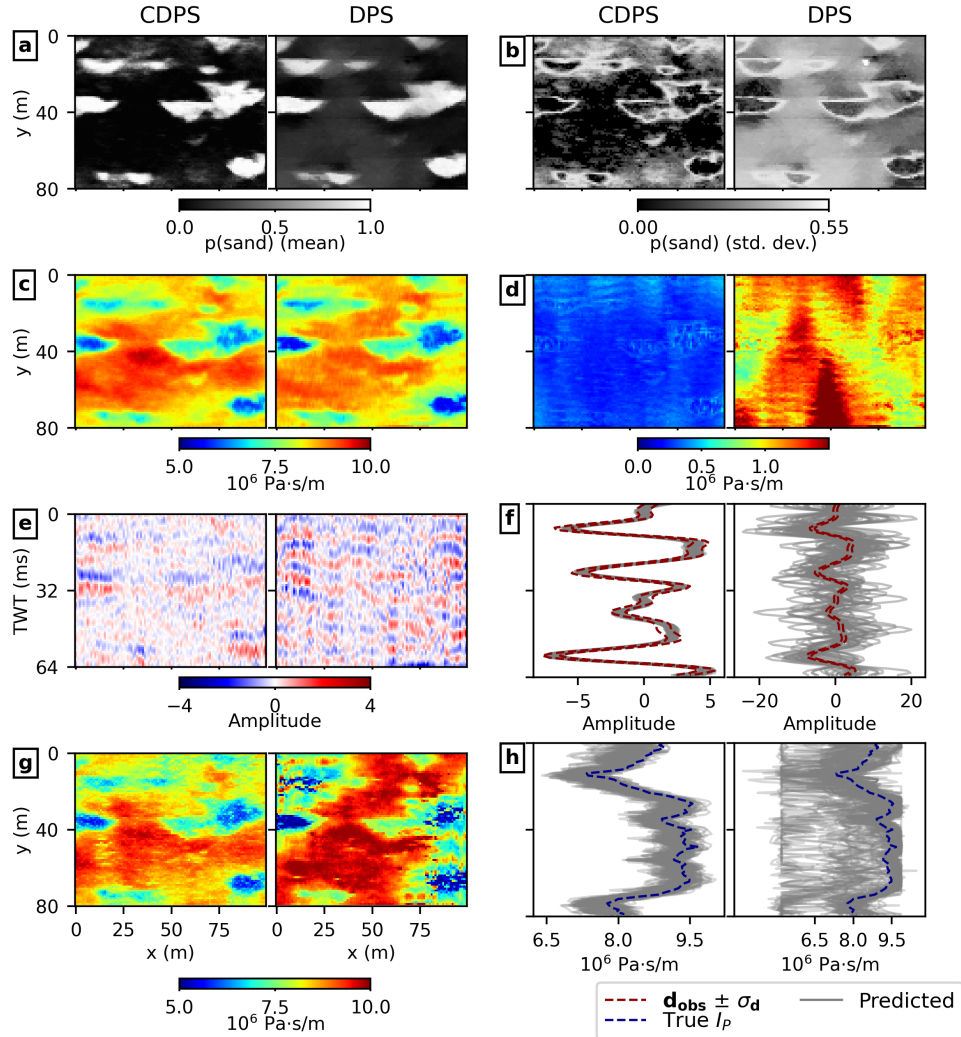


Figure 16: Sampled posterior distribution represented as (a) average facies; (b) facies standard deviation; (c) average I_P ; (d) I_P standard deviation; (e) average data error; (f) predicted data versus conditional data distribution ($d_{\text{obs}} \pm \sigma_d$) for a vertical trace at $x = 50\text{m}$; (g) I_P realizations; (h) I_P samples for a vertical trace at $x = 25\text{m}$ compared to the unknown target distribution.